Master's thesis

Master's Programme in Theoretical and Computational Methods

Mechanisms of exceptional radiation resistance of Ga_2O_3 by means of atomistic simulations of radiation damage in β-Ga_2O_3

Ru He

May 3, 2023

Supervisor(s): Prof. Flyura Djurabekova

Examiner(s): Prof. Flyura Djurabekova
Dr. Jesper Byggmästar

University of Helsinki
Faculty of Science

HELSINGIN YLIOPISTO — HELSINGFORS UNIVERSITET — UNIVERSITY OF HELSINKI

Tiedekunta — Fakultet — Faculty	Koulutusohjelma — Utbildningsprogram — Degree programme
Faculty of Science	Master's Programme in Theoretical and Computational Methods

Tekijä — Författare — Author

Ru He

Työn nimi — Arbetets titel — Title

Mechanisms of exceptional radiation resistance of Ga_2O_3 by means of atomistic simulations of radiation damage in β-Ga_2O_3

Työn laji — Arbetets art — Level	Aika — Datum — Month and year	Sivumäärä — Sidantal — Number of pages
Master's thesis	May 3, 2023	48

Tiivistelmä — Referat — Abstract

Ga_2O_3 has been found to exhibit excellent radiation hardness properties, making it an ideal candidate for use in a variety of applications that involve exposure to ionizing radiation, such as in space exploration, nuclear power generation, and medical imaging. Understanding the behaviour of Ga_2O_3 under irradiation is therefore crucial for optimizing its performance in these applications and ensuring their safe and efficient operation. There are five commonly identified polymorphs of Ga_2O_3, namely, β, α, γ, δ and ϵ structures, among these phases, β-Ga_2O_3 is the most stable crystal structure and has attracted majority of the recent attention.

In this thesis, we used molecular dynamics simulations with the newly developed machine learned Gaussian approximation potentials to investigate the radiation damage in β-Ga_2O_3. We inspected the gradual structural change in the β-Ga_2O_3 lattice with increasing doses of Frenkel pair implantations. The results revealed that O-Frenkel pairs have a strong tendency to recombine and return to their original sublattice sites. When Ga- and O-Frenkel pairs are implanted to the same cell, the crystal structure was damaged and converted to an amorphous phase at low doses. However, the accumulation of pure Ga-Frenkel pairs in the simulation cells might induce a transition of β to γ-Ga, while the O sublattice remains in the FCC crystal structure, which theoretically demonstrated the recent experimental finding that β- Ga_2O_3 transfers to the γ phase following ion implantation.

To gain a better understanding of the natural behaviour of β-Ga_2O_3 under irradiation, we utilized collision cascade simulations. The results revealed that the O sublattice in the β-Ga_2O_3 lattice is robust and less susceptible to damage, despite O atoms having higher mobility. The collision and recrystallization process resulted in a greater accumulation of Ga defects than O defects, regardless of primary knock-on atom type. These simulations further revealed that it is difficult for displaced Ga ions to return to the β-Ga lattice, while the FCC stacking of the O sublattice has very strong tendency to recover.

Our theoretical models on the radiation damage of β-Ga_2O_3 provide insight into the mechanisms underlying defect generation and recovery during experimental ion implantation, which has significant implications for improving the radiation tolerance of Ga_2O_3, as well as optimizing its electronic and optical properties.

Avainsanat — Nyckelord — Keywords

Ga_2O_3, irradiation, molecular dynamics, damage

Säilytyspaikka — Förvaringsställe — Where deposited

Muita tietoja — Övriga uppgifter — Additional information

Contents

1 Introduction **1**

2 Ga_2O_3 **Material** **3**

2.1 Property and Crystal Structure . . . 3

2.2 Radiation-Induced Defects . . . 4

2.3 Phase Transformation under ion irradiation . . . 6

3 Radiation Damage Simulation **11**

3.1 Primary Radiation Damage . . . 11

3.2 Molecular Dynamics . . . 13

3.3 Machine-Learning Interatomic Potentials . . . 15

4 Frenkel Pairs Simulations **17**

4.1 Simulation Method . . . 17

4.2 Analysis Methods . . . 18

4.2.1 Radial Distribution Function . . . 18

4.2.2 Defects Analysis . . . 18

4.2.3 Lattice Visualization . . . 18

4.3 Defects Visualization . . . 19

4.4 Radial Distribution Function Analysis of the Ga Sublattice . . . 20

4.5 Radial Distribution Function Analysis of the O Sublattice . . . 23

5 Single Cascade Simulations **27**

5.1 Simulation Method . . . 27

5.2 Analysis Methods . . . 28

5.2.1 Cluster Analysis . . . 28

5.3 Defects Formation . . . 28

5.4 Atoms Mobility . . . 33

5.5 Recoil Energy Dependence of Defects . . . 34

5.6 Defect Clustering . . . 35

6 Conclusions 39

Bibliography 41

1. Introduction

The development of wide bandgap semiconductors is of great importance in modern technology as they offer many advantages over traditional silicon-based semiconductors. Wide bandgap materials have a larger energy gap between the valence and conduction bands, which allows them to operate at higher temperatures, higher frequencies, and with greater efficiency than traditional materials. One such wide bandgap semiconductor that has recently gained attention is Gallium Oxide (Ga_2O_3). The development of Ga_2O_3-based devices could revolutionize power electronics, enabling higher power densities and reducing the size and weight of power conversion systems. Meanwhile, Ga_2O_3 has been found to exhibit excellent radiation hardness properties, making it an ideal candidate for use in a variety of applications that involve exposure to ionizing radiation, such as in space exploration, nuclear power generation, and medical imaging. Understanding the behavior of Ga_2O_3 under irradiation is therefore crucial for optimizing its performance in these applications and ensuring their safe and efficient operation. Besides, studying the irradiation effects also provide insights into fundamental aspects of materials science, such as defect formation and diffusion mechanisms, as well as the relationship between atomic structure and material properties.

Molecular dynamics (MD) simulations provide a powerful tool for gaining a deeper understanding of the physical mechanisms that dictate the behavior of materials subjected to radiation damage. By simulating irradiation damage at the atomic scale, researchers obtain critical insights into the behavior of materials under conditions that may be challenging or impossible to replicate experimentally.

The aim of the thesis is to investigate the structural stability of β-Ga_2O_3 under irradiation using MD simulations equipped with recently developed machine-learning potential [1]. The thesis is organized into six chapters. Chapter 1 introduces the motivation of the research. In Chapter 2 and 3, we describe the structural properties of Ga_2O_3 and its outstanding potential for industrial applications, basic concepts of primary radiation damage and basic principles of MD simulations. In Chapter 4, we describe the Frenkel pairs simulations to investigate the impacts of Frenkel pair defects on the structural stability of β-Ga_2O_3. To better understand the formation and migration of defects caused by radiation, in Chapter 5 we use collision cascade

simulations to analysis the radiation damage progress. In chapter 6, we summarize our results on the different radiation tolerance of Ga and O sublattices, and provide perspective of future work. The specific details related to the simulations presented in Chapter 4-6 are given in the first sections of the corresponding chapters.

2. Ga_2O_3 Material

2.1 Property and Crystal Structure

Wide-bandgap (WBG) semiconductors (bandgap > 3 eV) are extensively utilized in power electronic devices owing to their ability to reduce energy loss. So far, Silicon (Si) has been the primary material used in high-power device applications. Nonetheless, Silicon Carbide (SiC) and Gallium Nitride (GaN) have made remarkable progress in emerging domains like power controls, autonomous vehicle sensors, and multilevel converters. The development of next-generation electronics and photonics devices requires the use of semiconductors with ultra-wide bandgaps (UWBG), which are much wider than those of established materials. Fig. 2.1 shows the critical properties of usually reported WBG semiconductors materials. Ga_2O_3 is a better candidate for high voltage applications because of its large bandgap and lower cost. There are five commonly identified polymorphs of Ga_2O_3, namely, the monoclinic (β), rhombohedral (α), defective spinel (γ), cubic (δ), or orthorhombic (ϵ) structures, Table 2.1 illustrates their properties. Among these different phases of Ga_2O_3, the monoclinic (β-Ga_2O_3)phase structure is the most stable crystal structure and has attracted most of the recent attention. It has a wide band of about 4.8 eV with a high breakdown field of 8 MV/cm, exceeding traditional wide band materials such as SiC (3.3 eV) and GaN (3.4 eV) with a high predicted Baliga's merit value (BFOM) about 3444. BFOM is a crucial metric for assessing semiconductor materials that can be used in power devices [2][3]. Moreover, β-Ga_2O_3's high electron mobility and high transparency in the UV-visible range make it attractive for optoelectronics applications such as UV photodetectors and solar-blind photodetectors. This thesis is mainly focused on the research about β-Ga_2O_3, wishing to contribute for its further applications.

The monoclinic crystal structure of β-Ga_2O_3 is shown in Fig. 2.2, denoted as C2/m. The angle between a and c axes is 104°, and $a \perp c$, $b \perp c$[18]. As listed in the Table 2.1 the lattice parameters are$a = 12.12 \sim 12.34$ Å, $b = 3.03 \sim 3.04$ Å, and $c = 5.80 \sim 5.87$ Å. One unit cell contains four Ga_2O_3 polyhedrons, with two crystallographically different Ga (Ga1,Ga2) atoms and three distinct sites of O (O1,O2,O3) atoms. Ga1 atoms are bonded to four neighboring O atoms in a tetrahedral arrange-

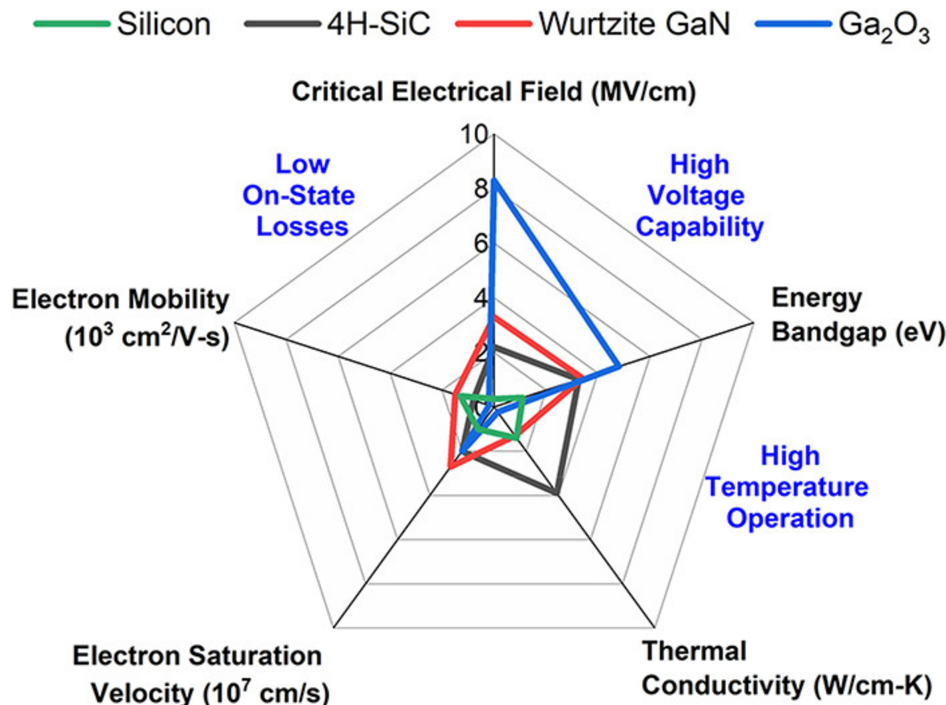

Figure 2.1: The pentagon diagram showing the critical material properties important to power semiconductor devices. A larger pentagon is preferred. The figure are taken from Refs.[4][5]

Table 2.1: Polymorph Properties of Ga_2O_3

Polymorph	Structure	Space Group	Bandgap Energy (eV)	Reference
α	Rhombohedral	R-3c	5.2-5.3	[6][7][8]
β	Monoclinic	C2/m	4.4-4.9	[6][9]
γ	Defective spinel, cubic	Fd-3m	4.5-5.0	[7][10][11][12]
δ	Body-Centered Cube	Ia3	Not available	[13][14]
ϵ	Orthorhombic	Pna2_1	4.6-4.91	[10][15][16][17]

ment. Ga2 atoms are in an octahedral environment and bind to six neighboring O atoms. O1 and O2 have threefold coordination, while O3 has fourfold coordination. The average distances between ions are listed as follows: Ga-O in a tetrahedral arrangement at 1.83 Å, Ga-O in an octahedral arrangement at 2.00 Å, O-O at the edge of a tetrahedron at 3.02 Å, and O-O at the edge of an octahedron at 2.84 Å[18][19].

2.2 Radiation-Induced Defects

Defects generated during the growth of materials or induced due to external exposure such as irradiation, ion implantation in semiconductors play a crucial role and significantly affect the material properties and device characteristics[20]. According to research, Si, Ge, and Sn on the Ga site, as well as F and Cl on the O site, have the potential to act as shallow donors, contributing to the intrinsic n-type conductivity of

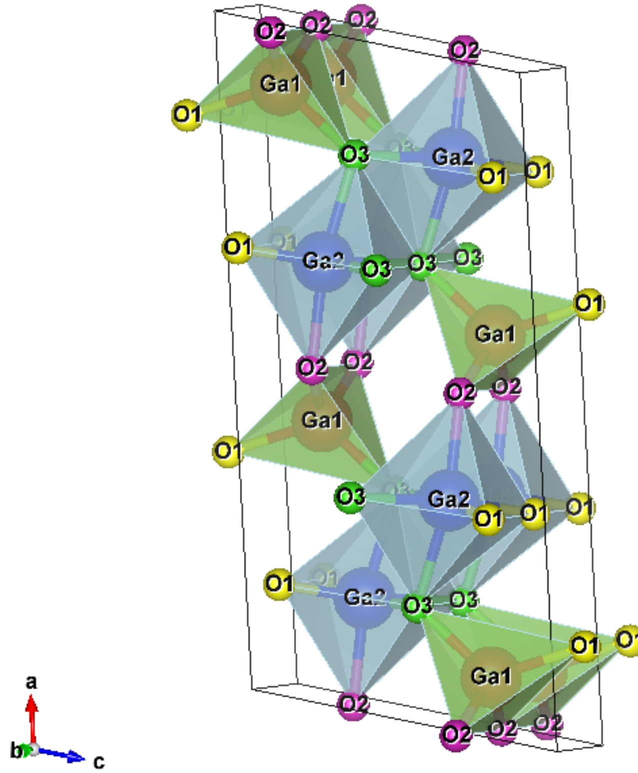

Figure 2.2: Crystal structure of β-Ga_2O_3

β-Ga_2O_3[21][22][23]. Furthermore, Ga vacancies play a compensatory role in this conductivity. Additionally, studies have shown that both O vacancies and Ga vacancies can cause Fermi-level pinning and adjust the work function of β-Ga_2O_3 in conditions of both O deficiency and O abundance[24][25].

The strong bonding in WBG materials makes them highly resistant to radiation. Ga_2O_3 has potential applications for photoconductors and electronics to be used in low earth orbit satellites or radiation-hard nuclear systems, which means devices could be subject to intensive fluxes of high energy protons, alpha particles and electrons, neutrons or gamma rays. At high incident energies, collisions between incoming particles and lattice atoms can lead to the creation of primary recoils with extremely high energies. These recoils can generate a cascade of collisions, resulting in the formation of heavily disordered regions or domains within the core [26][27][28][29]. When an energetic particle such as a neutron or proton collides with the nucleus of a lattice atom, it can displace the primary knock on atom from the from the lattice site. Fig. 2.3 shows atomic displacement damage in crystalline solid before and after exposure to radiation particles. The impact of an incoming ion on a lattice atom results in the displacement

of the atom from its original position, leading to the creation of vacancies, interstitials, and complexes of both in Ga_2O_3 .

Different forms of radiation produces different types of crystal lattice damage on the crystalline materials, which could critically influence properties of the device[30][31]. There are already multiple studies of the irradiation effects in Ga_2O_3 using alpha particles, neutrons, electrons, protons, swift heavy ion and gamma radiation with varying energies [32][33][34][35]. In addition, primary defects may recombine, and form complexes with each other. This may be more complicated in the case of β-Ga_2O_3 with the five different atomic sites atoms[36]. There is a larger number of possible defect complexes that could form in it upon irradiation. In order to ensure successful application, it is crucial to understand the mechanisms underlying the formation of radiation defects. This understanding can pave the way for future research aimed at controlling the defects.

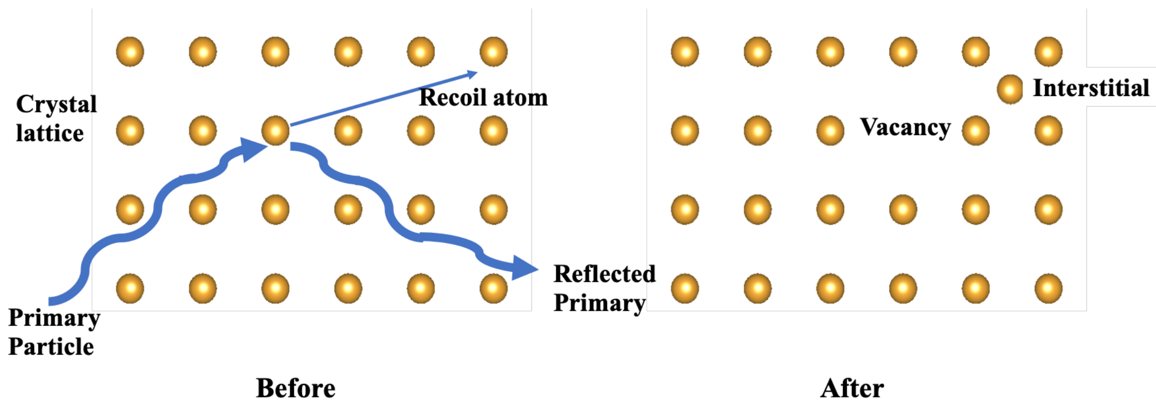

Figure 2.3: Schematic of atomic displacement damage in crystalline solid before and after exposure to radiation particles

2.3 Phase Transformation under ion irradiation

At room temperature and atmospheric pressure in air, the β-Ga_2O_3 is the thermodynamically stable polymorph, while other metastable polymorphs also possess favorable properties and can be stabilized using various methods. These methods include soft chemical synthesis techniques, high temperature and high pressure solid state synthesis, strain engineering in thin films, and ion implantation[37][38][39][40].

Among the aforementioned methods, ion implantation, which is irradiation of a material with energetic ions is a widely applied effective method to modify properties of materials, particularly in selective doping during the processing of electronic devices. Naturally, the energetic impacts inevitably create defects in the irradiated semiconductors by displacing the atoms from their equilibrium positions. Long irradiation with

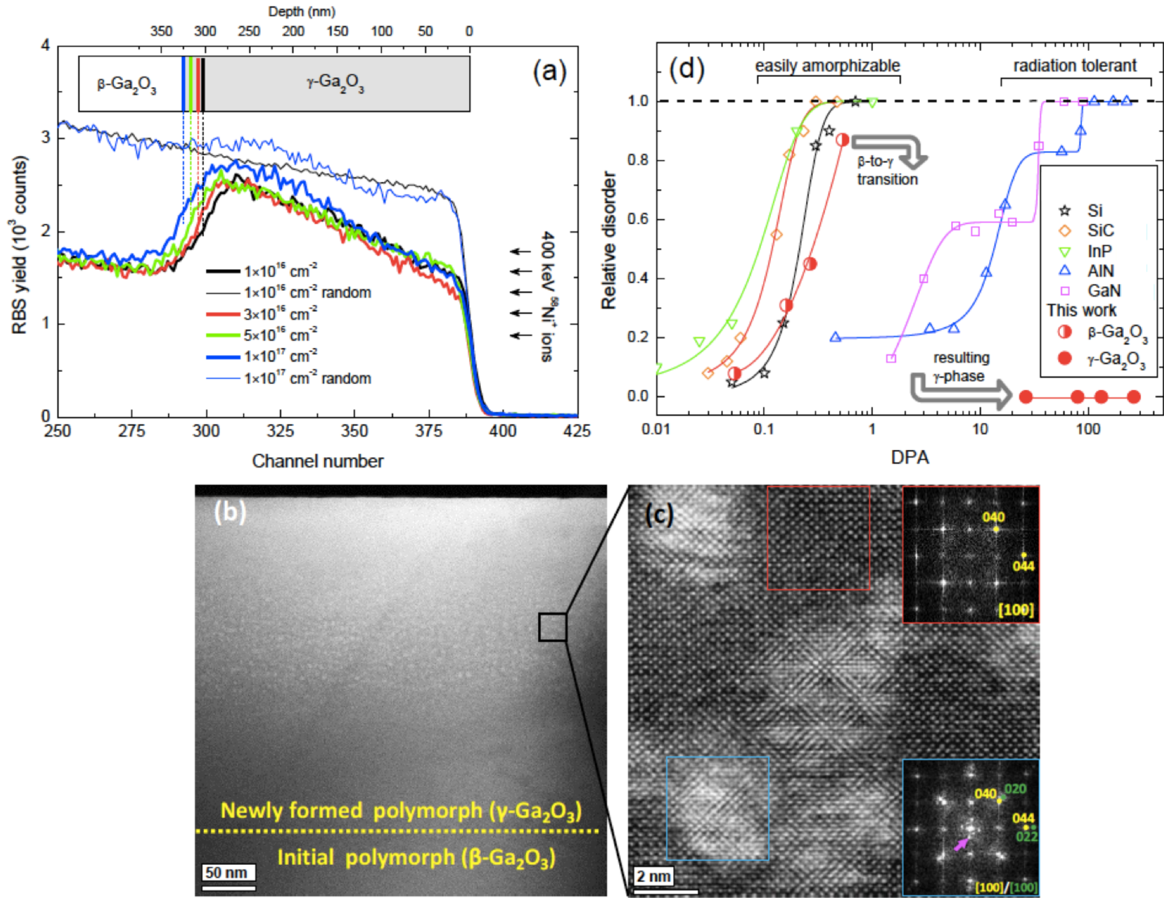

Figure 2.4: High radiation tolerance of the double γ-Ga_2O_3/β-Ga_2O_3 polymorph structures. (a) The Rutherford backscattering spectrometry in channeling mode (RBS/C) spectra of β-Ga_2O_3 samples implanted with 400 keV $^{5}8Ni^{+}$ ions to the different doses as indicated in the legend. (b) low magnification high-angle annular dark field -the scanning transmission electron microscopy (HAADF -STEM) image of the 1×10^{17} Ni/cm^2 sample showing full implanted region, (c) high resolution annular dark field - transmission electron microscopy (ADF-TEM) and corresponding FFTs of the areas with (blue) and without (red) Ni precipitates. γ-Ga_2O_3 planes are indicated in yellow, metallic Ni in green and double diffraction spots are indicated with a pink arrow; (d) relative disorder as a function of DPA for easily amorphizable and radiation tolerant semiconductors for Au implants at room temperature, as well as for Ga_2O_3. The figure is taken from Refs.[41].

energetic ions results in defect accumulation, which triggers local amorphization by creating localized regions of disordered structure and eventually, at high fluences (i.e. at sufficiently high number of ions per unit area), these lead to full amorphization of the irradiated material [42][43]. Sometimes, the formation of secondary phases is more gradual and is characterized by apperance of nanoscale inclusions[44][45]. Fig. 2.4d [41] evolution of structural disorder in typical semiconductors with dose. In the graph, the latter is another measure of irradiation in terms of so-called displacements-per-atom (DPA). This unit is used as a universal measure of irradiation which does not depend on energy or type of irradiating ions. On the left side of this graph we see disorder

evolution in common semiconductor materials, such as Si, SiC and InP, which are also known as easily-amorphizable. In some cases, however, the materials show high resistance to irradiation, remaining crystalline up to very high fluences. These materials are known as radiation-resistant and are considered for applications in particularly demanding environments. Particularly promising behavior is exhibited by AlN and GaN, which can be irradiated to fairly high doses before they turn fully amorphous. The mechanisms of such high radiation resistance are not fully understood yet, this is why, a thorough comprehension of the mechanisms behind defect formation and defect evolution due to ion irradiation is critical for advancement of modern electronic devices and the expansion of their capabilities.

A surprisingly high resistance of Ga_2O_3 to ion irradiation has been recently reported by Azarov et al.[41]. The authors saw that during irradiation of β-Ga_2O_3 by Germanium (Ge), Nickel (Ni), Gallium (Ga), or Gold (Au) ions to high fluences a new crystalline phase emerged instead of full amorphization as it would have been expected, if one follows the behavior of disorder evolution in this material shown by the red half-filled circles in Fig. 2.4d. At first, the authors saw the signature of high resistance of Ga_2O_3 while analyzing the Rutherford Backscattering Spectra in Channeling regime (RBS/C) from the irradiated β-Ga_2O_3 samples at different fluences. They noticed the significant difference between the spectra from an amorphous (random) and the damaged but still crystalline structures (compare blue thin and thick curves) at the same fluence of 10^{17} cm^{-2}, which is too high for a material to remain crystalline. The TEM analysis of the sample irradiated with Ni ions to this high fluence revealed high quality crystalline phase, which was different from crystalline Ni precipitates also formed during irradiation (see Fig. 2.4(b-c)).

The new phase was initially identified as a κ-Ga_2O_3 phase, based on the analysis of electron diffraction (SAED) patterns of selected areas in TEM. Later on, García-Fernández et al.[46] and Azarov et al.[41] revisited the experiment and alternatively identified the new phase as γ-Ga_2O_3 (see also Fig. 2.4a). The difference between two phases in greater detail is seen from the figure in Ref. [46] Fig. 2.5 shows the TEM image of the interface between the (201) oriented β-Ga_2O_3 and the transformed layer in the sample implanted with Silicon (Si). In conclusion, these experiments [41] show that initially β-Ga_2O_3 becomes disordered very similarly to other semiconductor materials, but at a certain dose of irradiation, the transformation to a new crystalline phase occur, which is highly tolerant to the much higher doses which none of the known materials were able to tolerate (see Fig. 2.4). This observation poses challenging question of mechanisms of such exceptional tolerance of Ga_2O_3. On the other hand, it is very attractive to develop a method to engineer formation of a metastable phase by controlling the atomic displacements that can lead to strain accumulation, but

experimental methods are too slow and expensive to look deep into atomic scale of the mechanisms that take place in this process. Hence atomistic dynamic simulations can become essential to study the resulting phase transformation in this complex modified for they may shed light on the precise mechanisms governing this process.

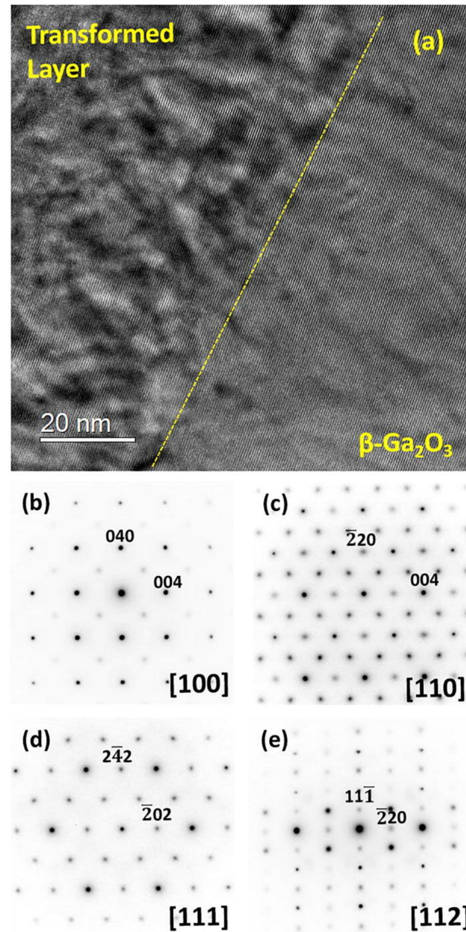

Figure 2.5: (a) Cross-sectional TEM image of the interface between the transformed layer and the (201) oriented β-Ga_2O_3 of the Si-implanted sample. SAED pattern of the transformed layer indexed according to γ-Ga_2O_3 along the zone axes (b) [100], (c) [110], (d) [111], and (e) [112]. The figure is taken from Ref.[46].

3. Radiation Damage Simulation

3.1 Primary Radiation Damage

Immediately following the impact of high-energy particles, primary damage is formed through atomic collision processes and intense material heating resulting from the non-equilibrium state of the colliding atoms. Scientific understanding of primary damage is the starting point in describing and predicting the radiation effects in materials[47][48]. When collisions occur during irradiation, a target atom may be displaced from its original position permanently if the transferred energy exceeds a certain threshold value, referred to as the threshold displacement energy (E_d). This value, which depends on the material, typically falls within the range of 20 to 100 electron volts (eV) [49]. Several computer simulations and experimental studies indicate that the time required for atom collision processes is approximately 0.1 $\sim$ 1.0 ps. Additionally, the time needed for the collisions to reach thermal equilibrium is around 1 $\sim$ 10 ps[50][51][52]. The typical stages of a collision cascade are shown in Fig. 3.1. The process begins with the initiation of the collision cascade by the primary knock-on atom (PKA), resulting in the formation of a region with an underdense core and dense fringes through the collision of atoms. During this stage, the atoms are in a disordered state, resembling a liquid phase. Subsequently, the dense outer regions initiate the recrystallization process into the low density core left behind. However, despite the recrystallization process, some defects remain within the system. The surviving displacements can take various forms, and some defects, along with their formation mechanisms, are discussed below.

- Frenkel pairs: Frenkel pairs (FPs) are formed when an atom is displaced from its normal lattice site and becomes an interstitial defect, leaving behind a vacant lattice site, which is a vacancy defect. These vacancy and interstitial defect are situated near each other while unable to recombine[53]. FPs are common in ionic crystals, where the cations and anions are of significantly different sizes, and cation vacancies and interstitials are prevalent[54]. They can play a critical role in the transport of ions through a crystal, as well as in the material's response to external stimuli such as radiation or temperature changes.

- Vacancy clusters: Vacancy clusters are formed when multiple adjacent vacan-

cies preferentially agglomerate due to the migration of vacancies, which move towards the recrystallization front during the recrystallization process. The size and shape of vacancy clusters can vary depending on the crystal structure and the conditions of the recrystallization process[55].

• Interstitial clusters: Interstitial clusters are formed when more than one interstitial atoms group together in the crystal lattice. Interstitial clusters can be generated during the collision cascade process, as the displacement of atoms can create interstitials. They can also be formed during the recrystallization process as the crystal lattice reforms and the displaced interstitial atoms meet and bond together. During a collision cascade, if the melted region assumes an elongated shape, the recrystallization process can prevent the recombination of excess interstitials which remain in the tip, while vacancies remain in the center. As a result, the excess interstitials are trapped, and interstitial clusters are formed. This mechanism is known as the "liquid-isolation" mechanism [56]. The size and shape of interstitial clusters can vary depending on the crystal structure and the conditions during the formation process[57].

• Dislocation loops: Dislocation loops are formed when a dislocation line forms a closed loop within the lattice[58]. In high-energy collision cascades, such as in some materials tungsten (W) or iron (Fe), both interstitial-type and vacancy-type dislocation loops can form[59][60].

• Amorphous clusters: Amorphous clusters are clusters of atoms or molecules that lack a long-range ordered structure, and are instead arranged in a disordered, or amorphous, manner[61]. Observations of amorphous clusters have been made in semiconductors such as silicon (Si) and germanium (Ge) [56]. This is attributed to weaker defect annealing in semiconductors compared to metals, which is caused by different types of bonds [62].

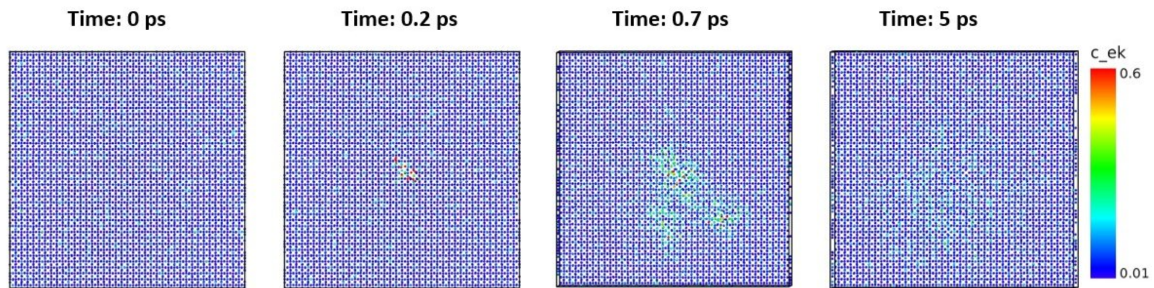

Figure 3.1: Example cascade in β-Ga_2O_3 with 1.5 keV PKA-energy: Kinetic energy of atoms during a collision cascade

As the collision cascades of atoms is extremely fast and far from equilibrium, the experiment observation of primary damage at the time scale is nearly impossible.

Computer simulations become the most promising method for the research of primary radiation damage during the past decades. In Fig. 3.2, multiscale physics and modelling of radiation effects in materials are listed. The boxes provide a rough indication of the suitable range of application for each method. In a perfect scenario, density functional theory (DFT) calculations would offer an accurate portrayal of the primary damage and subsequent development of collision cascades within simulation methods. Nonetheless, due to the current computational limitations of the DFT approach, it is impractical for addressing large-scale problems that require models capable of providing realistic, explanatory, extensible, or predictive insights into defect generation. As a result, molecular dynamics simulations employing analytical potentials have emerged as the predominant approach for simulating primary damage in materials, as they offer access to considerably larger time- and length-scales than those achievable with DFT.

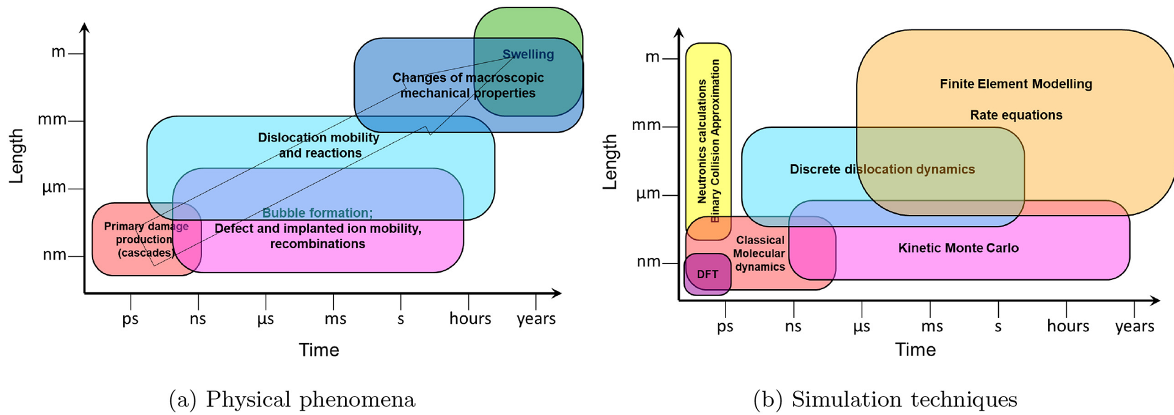

(a) Physical phenomena

(b) Simulation techniques

Figure 3.2: a) Multiple scales of physical phenomena b) Multiscale modeling to address this. The figure is taken from Ref.[48] and Ref.[63]

3.2 Molecular Dynamics

Molecular Dynamics (MD) is a powerful computational technique that utilizes Newton's equations to simulate the motion and interactions of atoms and molecules. Over recent years, MD has emerged as an essential tool for scientific research across multiple fields, including physics, chemistry, materials science, and biology. By providing a detailed depiction of molecules and atoms' behavior under various conditions, such as temperature, pressure, and concentration, it offers insight into the underlying principles governing chemical and physical processes. Here, a brief introduction is given on the basic concepts of MD simulation.

Fig. 3.3 shows the typical MD algorithm. In the beginning of the simulation, the initial positions, velocities of all atoms or molecules in the system are set according to a given starting configuration. This can involve reading in a file with the starting

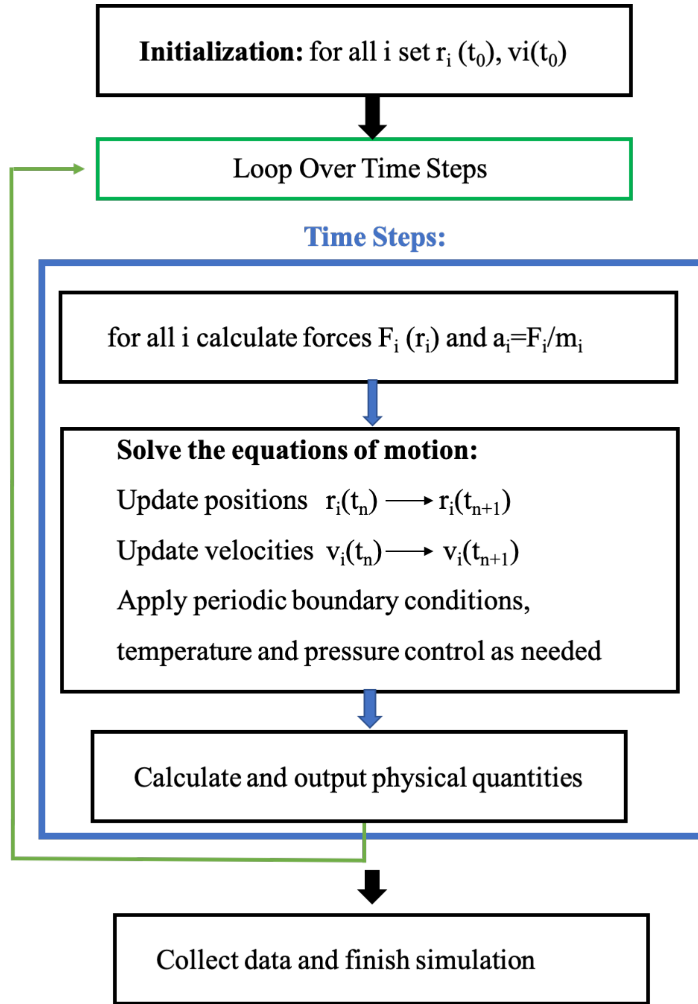

Figure 3.3: Simplified schematic of the MD algorithm

positions, randomly generating positions, or using experimental data. To initiate the evolution of the system, the force acting on each atom is calculated. The force acting on each atom is calculated from the gradient of potential energy. The relationship between the force (F_i), and the interatomic potential ($V(r_i)$) for each atom is:

$$F_i = -\nabla_{r_i} V(r_i)$$

where ∇_{r_i} is the gradient operator with respect to the position vector of the i-th atom (r_i). Each atom's acceleration be calculated according to Newton's equation of motion with a suitable integrator algorithm like Velocity Verlet[64]. MD becomes quickely expensive with increasing system size. Periodic boundary conditions (PBC) is employed to simulate the behavior of materials inside the bulk. This means that an atom leaving the cell from one side (+x/y/z) will come back from the opposite side (-x/y/z)

The time step Δt is essential to any numerical solver algorithm for the integration

of motion equations. It should be chosen carefully to make it small enough that the system can represent physically properties reliably and large enough that the simulation does not become too slow. In case of irradiation simulations, an adaptive time step is used. When the system contains energetic particles, Δt tends to decrease, and as the temperature decreases, Δt tends to increase[65][66]. In the adaptive time step, Δt is chosen according to following equation:

$$\Delta t_{\text{new}} = min(\frac{\Delta x_{\text{max}}}{v_{\text{max}}}, \frac{\Delta E_{\text{max}}}{F_{\text{max}} v_{\text{max}}}, 1.1\Delta t, \Delta t_{\text{max}})$$

Here, x_{max} is the largest distance allowed to move during Δt, E_{max} is the maximum energy change, F_{max} and v_{max} is the maximum force acting on any atom and highest speed, respectively. Δt_{max} is the maximum time step allowed.

The simulation cell is coupled with a heat bath to remove excess energy from the system deposited by an incoming ion or an energetic recoil or maintain the initial system to some equilibrium temperature. It is done by applying a thermostat algorithm, for instance Nosé-Hoover thermostat which was introduced by William Graham Hoover and Anderson Rossini Nosé in 1984[67]. The algorithm uses an extended system of equations of motion to maintain a constant temperature by adjusting the system's energy fluctuations.

3.3 Machine-Learning Interatomic Potentials

As forces are calculated based on the interatomic potential energy function, the interatomic potential which defines the interactions between atoms and molecules within the system is a critical component of MD simulations. The choice of potential depends on the specific system being studied and the level of accuracy required. For example, simple potentials like the Lennard-Jones potential may be sufficient for studying simple liquids[68], while more complex potentials such as the CHARMM force field or AMBER force field are often used for studying biomolecules[69][70]. Accurate potentials are essential for reproducing experimental observations and providing insight into the underlying physical and chemical processes governing the system's behavior. In an ideal situation, interatomic forces would be calculated using quantum mechanical models. However, these models can become computationally impractical very quickly. Therefore, to create an efficient MD model, the interatomic potential should be as simple as possible without compromising its physical accuracy in describing the system's effects.

Machine-Learning (ML) interatomic potentials are a class of computational models that utilize machine learning algorithms to approximate the interatomic potential

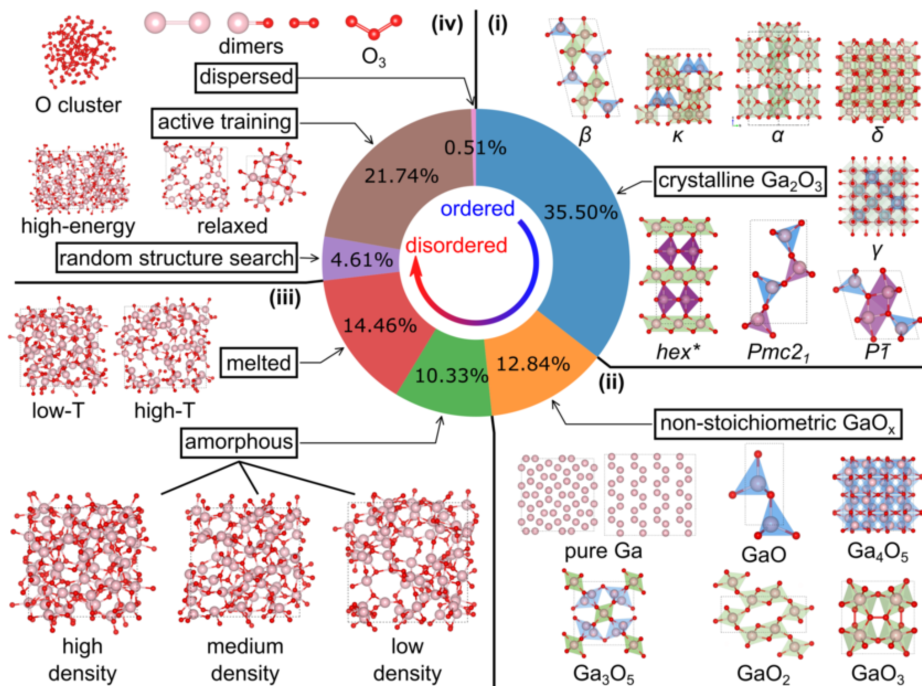

Figure 3.4: An overview of the DFT database. The fractions of the configuration-type-specific atom numbers to the total number (108,411) of atoms in the database are shown in the central part of the donut chart. For different configuration types, representative structures are shown as examples. In the panels (i) and (ii), the colored polyhedral within the crystalline structures show the 4-fold (blue)/5-fold (purple)/6-fold (green) Ga sites. Note that the isolated Ga and O (not shown here) are also included in the database as the global references of potential energies. The figure are taken from Ref.[1]

of a given system. By leveraging large amounts of data generated from density functional theory, ML interatomic Potentials can capture complex non-linear relationships between atoms and molecules' positions and their corresponding forces. Unlike traditional interatomic potentials, ML Interatomic Potentials can capture system-specific behavior without requiring explicit functional forms, making them versatile and adaptable to a wide range of materials and conditions. However, the accuracy of data-driven ML interatomic potentials is highly dependent on the consistency and comprehensiveness of the input data.

A general-purpose tabulated low-dimensional ML gaussian approximation interatomic potentials (tabGAP) was recently developed by Zhao, Junlei et al.[1]. Fig. 3.4 illustrates training database and the corresponding structures utilized for the development of their potential. The input data sets composed of energies and forces of a range of configurations which generated by DFT calculations. To ensure the generality of the potential, a wide range of Ga-O structures are included. In this thesis, the newly developed potential was employed for all the MD simulations about β-Ga_2O_3.

4. Frenkel Pairs Simulations

4.1 Simulation Method

MD simulations are commonly employed to investigate radiation damage. Traditionally, these defects are obtained in MD simulations by emulating primary knock-on atoms (PKAs) and simulating collision cascades, followed by examining the overlap of these cascades to observe the evolution of defects[71][48]. However, this approach can be computationally expensive if high irradiation doses are needed, as the numerical evaluations in MD simulations require small timesteps to ensure stable behaviors of atoms with high velocities. In this chapter, radiation-induced defects in MD cells were created using the Frenkel pair implantation method. This approach involves introducing Frenkel pair defects, directly into the system, bypassing the need to simulate a collision cascade. The classical MD code LAMMPS[72] was utilized to run the simulations, with the newly developed ML interatomic potential (tabGAP) for the Ga_2O_3 system[1] being employed.

In this chapter, we used Frenkel pairs accumulation (FPA) simulations, to investigate the impact of irradiation damage on the cation and anion sublattices in β-Ga_2O_3. A β-Ga_2O_3 simulation cell with the periodic boundary conditions and 1280 atoms was used for these simulations, and various numbers of Ga and Oxygen (O) FPs were implanted in the cell. The study comprised of three separate simulations. In the first two simulations, the pure Ga and O FPs were created iteratively by randomly displacing an ion of the corresponding type in a direction determined randomly with a distance of approximately 6 Å. In the last simulation, FPs were introduced iteratively in another cell by displacing an ion without considering its atom type to examine the influence of the mixed damage between sublattices. After each Frenkel pair was introduced, the simulation cell was relaxed to reach the local energy minimum and to prevent possible atom overlap. Subsequently, NVT-MD was performed using an adaptive timestep for a duration of 5 ps at a temperature of 300K to thermally equilibrate the system.

4.2 Analysis Methods

4.2.1 Radial Distribution Function

The radial distribution function (RDF) is listed bellow:

$$g(r) = \frac{\rho(r)}{N_{\text{at.}}/V}$$

where $\rho(r)$ is the density within a thin spherical shell of radius r, $N_{\text{at.}}$ is the total number of particles, and V is the system cell volume. When the system is amorphous, the function plot is close to 1 at long-range distances. Crystals have regular, periodic structures, with atoms fluctuating near their lattice positions. Discrete peaks occurred in RDF function plot are determined by the structure of the crystal[73]. Thus, the partial radial distribution functions (PRDF) can be used to characterize the structure of type-specified sublattice structures in a multispecies system[74].

Pearson correlation coefficient (Pr) was used to measure the similarity in terms of strength and direction of the linear correlation between two RDF curves, according to the formula:

$$Pr = \frac{\sum_{i=1}^{n}(x_i - \bar{x})(y_i - \bar{y})}{\sqrt{\sum_{i=1}^{n}(x_i - \bar{x})^2 \sum_{i=1}^{n}(y_i - \bar{y})^2}}$$

Where x_i and y_i are the variable samples of the two curves, respectively. $\bar{x}$ and $\bar{y}$ are the means of x and y respectively.

4.2.2 Defects Analysis

The Wigner-Seitz method partitions space around each atom into Voronoi polyhedra, which are used to identify point defects such as vacancies, interstitials, and FPs [75]. Ovito [76] was used to analyze simulation results and identify defects using the Wigner-Seitz method.

4.2.3 Lattice Visualization

The β-Ga_2O_3 lattices that contained accumulations of FPs are visualized with Ovito[76]. The crystal structures of the O sublattice in β-Ga_2O_3 lattices were analyzed using Ovito's common neighbor analysis tool during the visualization process.

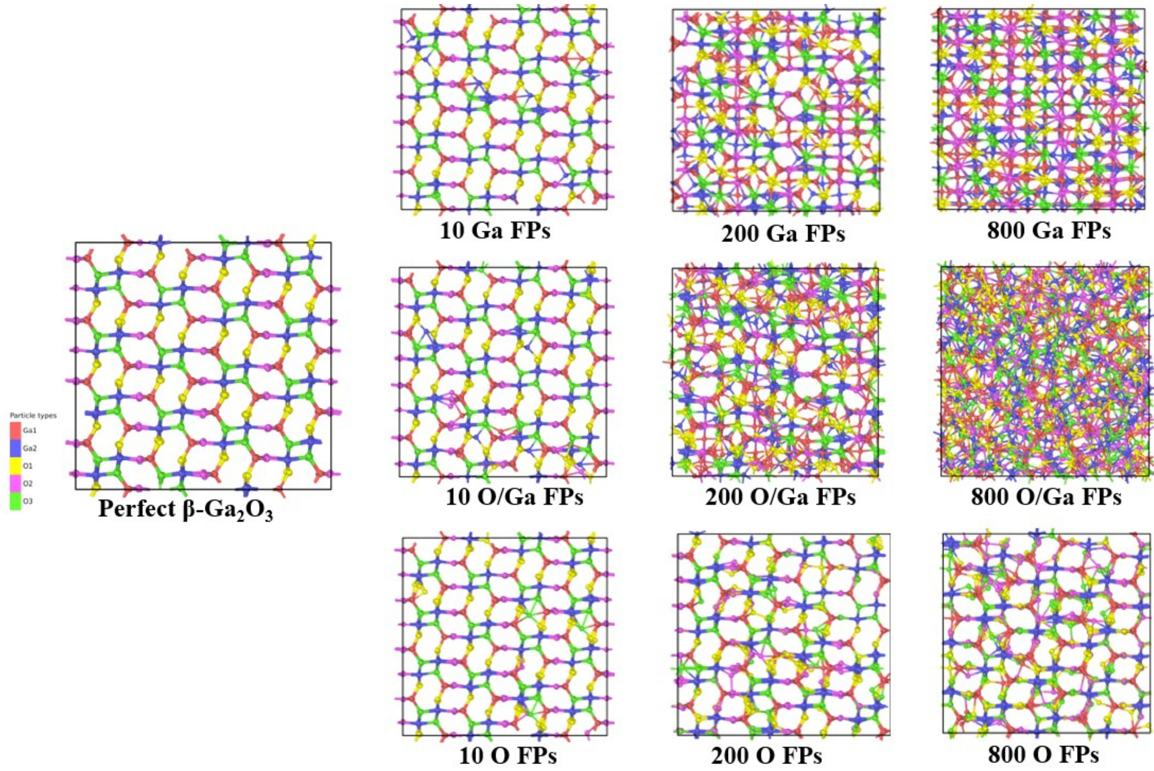

Figure 4.1: The snapshots show modifications of the pristine β-Ga_2O_3 lattices after introducing different amounts and types of FPs. (The ions located in five distinct sites in β-Ga_2O_3 are colored separately. Ga1 ions are shown in red, Ga2 ions are shown in blue, O1 ions are shown in yellow, O2 ions are shown in pink, O3 ions are shown in green.)

4.3 Defects Visualization

Long-range periodicity is exhibited by crystal phases and the crystal structure determines many of the physical and chemical properties of the crystal, including its density, melting point, optical properties, and electrical conductivity. Fig. 4.1 shows the pristine β-Ga_2O_3 lattices changes with increasing number of FPs of different types (from top to bottom): pure Ga FPs, mixture of Ga and O FPs (Ga/O) and pure O FPs, respectively. We see very little change in the structure of β-Ga_2O_3 after introducing 10 FPs independently of the type. When introducing 10 O FPs, we observe fewer surviving defects than in the cell with other types of FPs. Increasing number of FPs exhibits interesting behaviour in the simulation cells with different types of FPs. In the simulation cells with 200 and 800 pure Ga FPs, we still observe an ordered structure, and as the number of FPs increases, the unit cells become denser. However, it cannot been identified as β-Ga_2O_3 crystal structure by the eye. Increasing the number of O FPs to 800 does not notably change the original structure. The simulation cell with 800 O FPs closely resembles the original β-Ga_2O_3, except for the presence of defects. For the lattices with O/Ga FPs, the crystal structure deteriorated rapidly with the

number of randomly added Ga and O FPs increased. As more mixed type of FPs were introduced, the pristine β-Ga_2O_3 lattice underwent a gradual transformation into an amorphous phase.

4.4 Radial Distribution Function Analysis of the Ga Sublattice

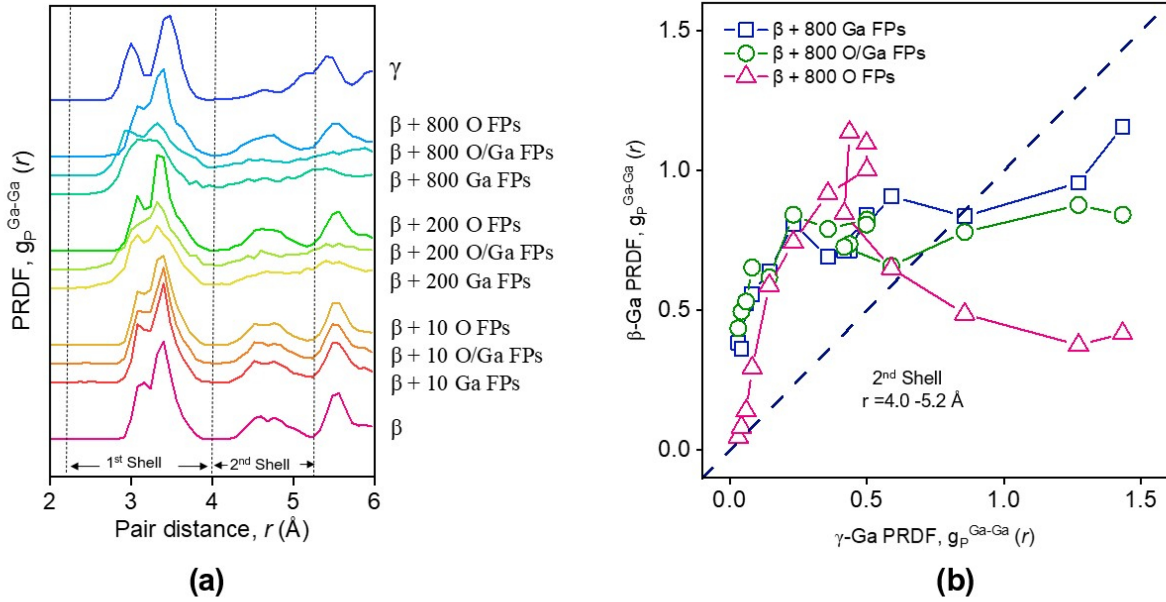

Figure 4.2: Analysis of the PRDFs of Ga sublattices with different amounts and types of additional FPs in β-Ga_2O_3 lattices :(a) Ga-Ga PRDFs for the pristine β-Ga_2O_3 lattice (down); up from the pristine Ga-Ga PRDFs, the same PRDFs for lattices with increasing numbers of pure Ga FPs, O/Ga FPs and pure O FPs; Ga-Ga PRDFs for the pristine γ-Ga_2O_3 lattice (up). (b) The similarity of the PRDF values of the β-Ga_2O_3 with 800 different types of FPs versus the PRDF of the pristine γ-Ga within the 2nd shell.

PRDF can be described as a structural property fingerprint that captures the characteristics of a sublattice. We applied successfully such an analysis to identify the gradual changes in the β-Ga sublattice due to subsequent addition FPs already in Ref. [41]. Now, we further analyze in Fig.4.2 (a) this effect by following the changes in the Ga-Ga PRDFs versus the accumulation of FPs by a specific type, which was not yet done previously. More specifically, Ga-Ga PRDF features can be considered separately within so-called the 1st (2.2 - 4.0 Å) and 2nd shell (4.0 - 5.2 Å). By comparing the PRDFs of the pristine β- and γ-Ga_2O_3 lattices, it becomes evident that a distinct feature within the 2nd shell is only present in β-Ga_2O_3, which exhibits peaks at approximately 4.5 Å. There are no peaks in the 2nd shell PRDF of γ-Ga_2O_3 (the topmost curve in Fig.4.2(a)). Here we see similarly to our previous work[41] that with increase of the number

of the Ga FPs in a pristine β-Ga sublattice, this feature gradually vanishes and the PRDF of the β-Ga attains shape closer to that of the γ-Ga. When introducing only O FPs, the peaks within the second shell remain visible, even with 800 O FPs. If FPs are added randomly without considering the ion type, the feature also gradually disappears. To quantitatively analyze the observed similarities in the curve, Fig.4.2 (b) plots the PRDF values in the second shell of the damaged β-Ga with 800 FPs of three different types: pure O, Ga, and a mixture of O/Ga FPs, against the PRDF of the pristine γ-Ga within the same interatomic distance range. In these plots, we can see that the PRDF of the damaged β phase is the closest to the γ-Ga, if only Ga FPs were introduced in the simulation cell. Mixing the ion type of FPs is reducing the similarity of the two curves, especially at the larger values of $g(r)$ of the γ-Ga sublattice. This deviation even stronger for the β-Ga sublattice, if only O FPs are introduced: two curves clearly have their largest values at different distances. We conclude that the transition from β-Ga to γ-Ga sublattices take place largely due to formation of Ga FPs. Formation of O FPs does not trigger this transition even after large number accumulation of these defects.

Table 4.1: Pearson correlation coefficients (Pr) within the 2nd shell for the PRDF of damaged β-Ga and the pristine β-Ga

Amount of FPs	Pr (O FPs)	Pr (O/Ga FPs)	Pr (Ga FPs)
10	0.978	0.975	0.969
200	0.960	0.267	0.219
800	0.886	0.097	-0.148

Table 4.2: Pearson correlation coefficients (Pr) within the 2nd shell for the PRDF of damaged β-Ga and the pristine γ-Ga

Amount of FPs	Pr (O FPs)	Pr (O/Ga FPs)	Pr (Ga FPs)
10	-0.042	0.093	0.063
200	0.039	0.851	0.918
800	0.175	0.881	0.942

Furthermore, to illustrate the similarities of the PRDF of the damaged β-Ga to γ-Ga sublattices, the Pearson correlation coefficients (Pr) were computed between the Ga-Ga PRDFs of the β-Ga with 10, 200 and 800 FPs of various types and those of the pristine β- and γ- Ga. The resulting coefficients are listed in the Table 4.1 and 4.2. The Pearson correlation analysis of the PRDFs of the β-Ga with different Ga FPs displayed high degree of positive correlation with the PRDF of γ-Ga. However, when the same analysis was applied for the PRDF of β-Ga, notable deviations from the original structure were observed. Comparable outcomes were observed when introducing

mixed FPs. Upon the addition of 800 O/Ga FPs, the Pr value of the PRDFs for γ-Ga is 0.881, which is smaller than the corresponding Pr value changed with 200 Ga FPs (0.918). This means that if the β-Ga_2O_3 lattice has extra O FPs, the higher level of the Ga FPs accumulation was required for the transformation of β- to γ-Ga. The analysis of Pearson correlation on the PRDFs of β-Ga with O FPs indicated that O defects have a lesser impact on the damage of the Ga sublattice.

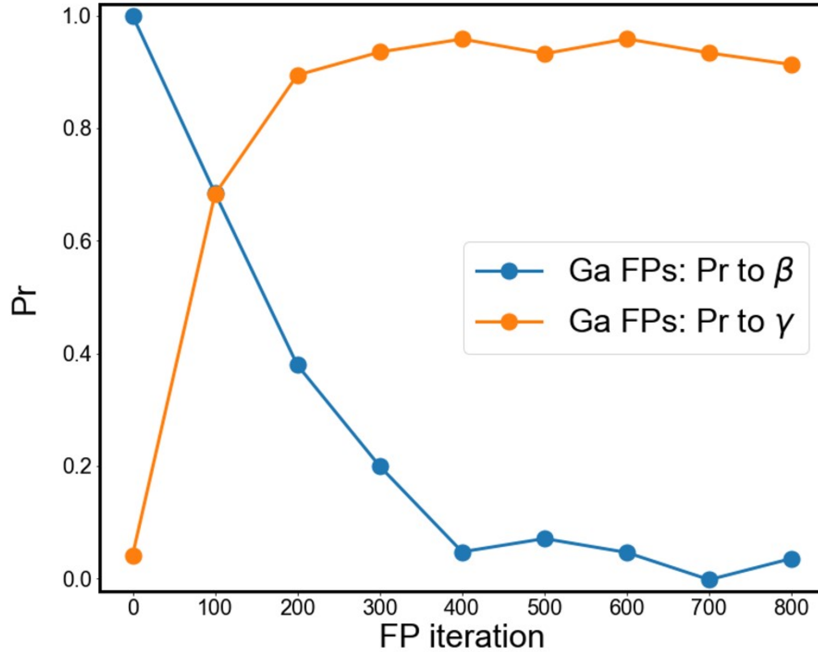

Figure 4.3: The Pearson correlation coeffient, Pr, calculated within the 2nd shell for the PRDF of the increasingly damaged β-Ga with respect to the pristine β-Ga and γ-Ga PRDFs as a function of the number of the pure Ga FPs.

As Ga FPs trigger the phase transformation from β- to γ-Ga sublattices, we plot the Pearson correlation coefficients for the PRDF of the increasingly damaged β-Ga sublattice with the growing number of the pure Ga FPs, as compared to the pristine β-Ga and γ-Ga PRDFs to study the phase transition threshold. The plots in Fig. 4.3 show that approximately 100 Ga FPs introduced into the cell, which corresponds to the displacements of 0.20 (of Ga ions) per Ga atom (dpGa), triggers inevitable transformation of the β-Ga sublattice into the γ-Ga sublattice. Upon surpassing the threshold number of Ga FPs, the PRDF of the damaged β-Ga exhibits a significantly greater similarity to the PRDF of the γ-Ga phase than that of the original β-Ga phase. When 200 Ga FPs (0.4 dpGa) were introduced into the simulation cell, the damaged β-Ga sublattice becomes noticeably similar with the γ-Ga. The results indicate that β-Ga gradually transforms into a γ-like phase when the number of Ga FPs increases to 200 (corresponds to the dose of 0.4 dpGa), and maintains the γ-like phase when the number of Ga FPs is even higher.

4.5 Radial Distribution Function Analysis of the O Sublattice

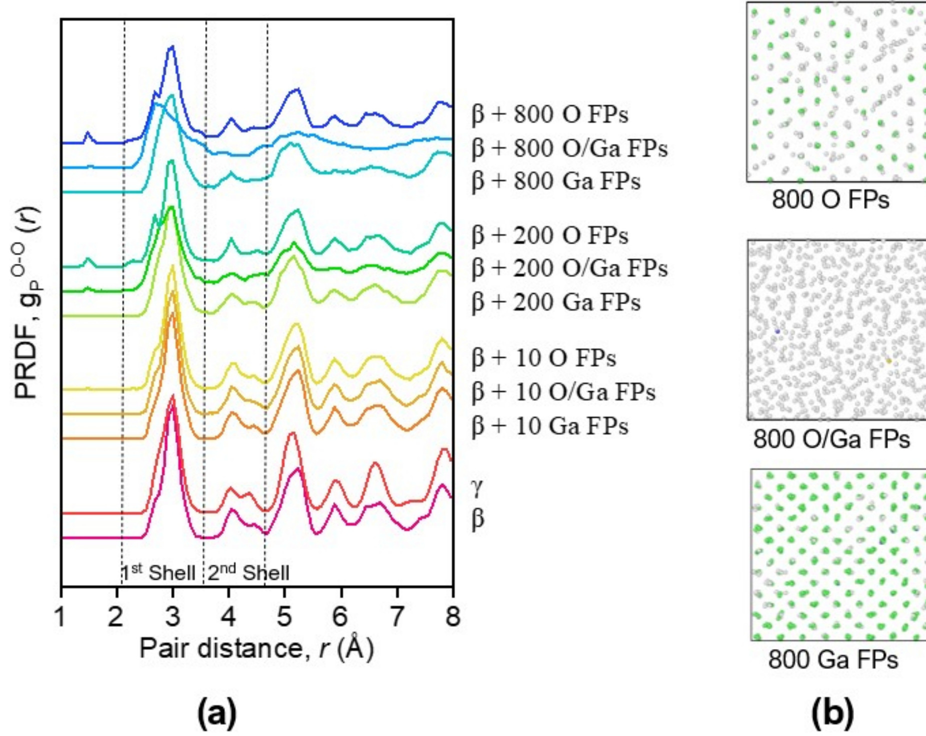

Figure 4.4: Analysis of the PRDFs of O sublattices with different amounts and types of additional FPs in β-Ga_2O_3 lattices :(a) O-O PRDFs for the pristine β- and γ-Ga_2O_3 lattice (down); up from the pristine O-O PRDFs, the same PRDFs for β-Ga_2O_3 lattices with increasing numbers of pure Ga FPs, O/Ga FPs and pure O FPs. (b) The snapshorts of structure analysis for the O sublattice in β-Ga_2O_3 with 800 pure O, Ga and mixture O/Ga FPs (the green color is used for O ions belong to Face Centered Cubic (FCC) crystal structure, grey is used for O ions belong to other structure which are non-classified ions).

In our previous work [41], we focused on the Ga-Ga PRDFs of the damaged β-Ga_2O_3 lattice. However, the behaviour of oxygen sublattice under higher dose irradiation has not been studied in detail. In this section, we analyze the O-O PRDFs of the damaged β-Ga_2O_3 lattice via introducing FPs and demonstrate the changes occurring in the oxygen sublattice. The oxygen sublattices in both the β- and γ-Ga_2O_3 materials share the same face-centered cubic (FCC) crystal structure. Fig. 4.4 (a) exhibits the O-O PRDFs of β- and γ-Ga_2O_3 shown as the bottom two curves, respectively. The comparison of these curves immediately reveals a substantial resemblance between them. The modifications observed in the O-O PRDFs, in relation to the accumulation of various types of FPs, are depicted in Fig. 4.4 (a). To be more specific, the O-O PRDFs are separated into two segments: the first shell (2.0-3.6 Å) and the second shell

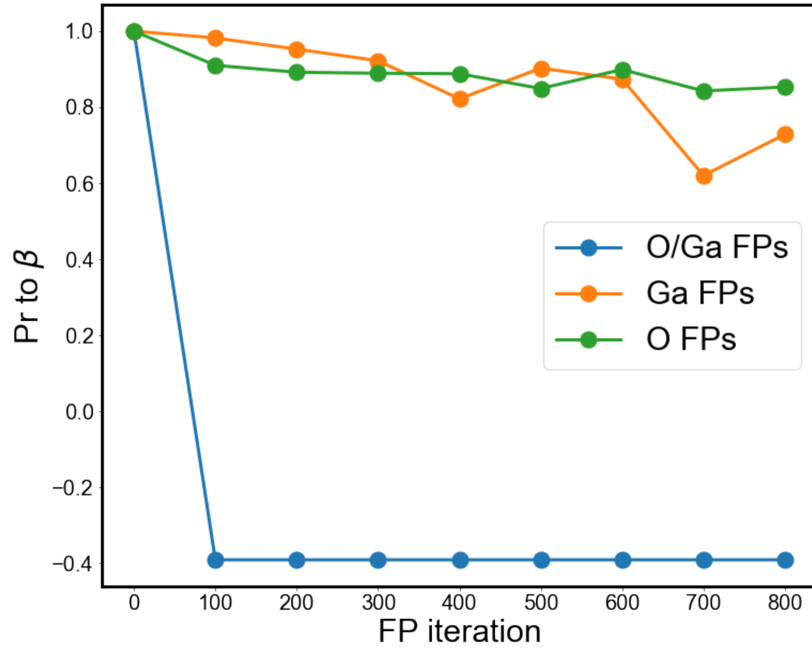

Figure 4.5: The Pearson correlation coefficient, Pr, calculated within the 2nd shell for the O-O PRDFs of the increasing damaged O sublattice with respect to the pristine β-O PRDFs as a function of the FP number.

(3.6-4.6 Å). As the number of pure Ga FPs increases in the β-Ga_2O_3 lattice, the peaks in the O-O PRDFs become broader, the main peaks remain present. Upon the inclusion of solely O FPs, the peaks observed in the O-O PRDFs exhibited a similar trend as that observed in the presence of Ga FPs. However, the peaks retained their sharpness more effectively than when the same quantity of Ga FPs was added. Following the addition of 800 O FPs, the O-O PRDFs clearly exhibited the characteristic peaks of the original FCC structure. With the introduction of random mixture O/Ga FPs, the peaks present in the O-O PRDFs rapidly transition towards a drum-like shape and approach the RDF curve of an amorphous structure when O/Ga 800 FPs are added. Upon the artificial introduction of O FPs, small peaks were observed around 1.47 Å, indicating the generation of O-O bonds. However, even with the generation of O defects due to changes in the FCC structure after adding extra Ga FPs, the O ions did not come closer to each other and thus avoided the formation of strong O-O bonds. To improve comprehension of the structural alterations occurring in the O sublattice due to the presence of the high number of FPs, Fig. 4.4 (b) illustrates snapshots of the structure analysis conducted on the O sublattice of β-Ga_2O_3 with 800 pure O, Ga, and O/Ga FPs (where green indicates O ions that belong to the FCC lattice, and grey indicates O ions that cannot be identified as occupying the FCC sites, but as defects). Despite the accumulation of the high number of the pure Ga and O FPs, the O sublattice remains fairly ordered. However, in the presence of O/Ga mixture FPs, the FCC

structure of O sublattice is completely destroyed, and the sublattice undergoes a phase transition to the amorphous phase. It appears that Ga defects facilitate the movement of O ions away from their original positions, resulting in the rapid destruction of the crystal structure.

For quantitative analysis of the damage of the O sublattice, we plotted the Pearson correlation coefficient of the O-O PRDFs in the 2nd shell for the damaged structures as compared to the pristine β-O structure with the increasing number of FPs in Fig. 4.5. When pure type FPs were added, the O-O PRDFs display a high degree positive correlation with the β-O structure, indicating a high level of structural similarity. The Pr values for pure O and Ga FPs implantation are fluctuating and close to each other with increasing defect concentration. After approximately 700 Frenkel pair iterations, Ga defects appear to cause more damage to O sublattice than O defects, and maintained a relatively high similarity to the perfect β-O structure, the corresponding Pr value is around 0.73. In the case of introducing mixture of FPs, the Pr value dramatically decreased to negative values, indicating complete damage to the O sublattice with lower concentrations of mixed FPs. This further supports the idea that Ga interstitials could block displaced O ions and prevent their recombination to the FCC lattice sites.

5. Single Cascade Simulations

5.1 Simulation Method

The previous chapter discusses the influence of various types of FPs on the Ga and O sublattices. In natural irradiation scenarios, it is not possible to generate only Ga or O FPs at the atomic scale. Therefore, to gain a better understanding of the effects of irradiation on β-Ga_2O_3, this chapter presents the results of the single cascade simulations.

The single cascades were run using LAMMPS [72] and the ML interatomic potential (tabGAP) developed by Junlei Zhao et al[69]. Cascades were initiated by giving to a randomly chosen atom, which is known as primary knock-on atom (PKA), the recoil energy. The initial momentum direction and position of a PKA was chosen randomly from the center area of the simulation cell. As recoil energy increases, the cascades become more extensive. For the cascade not to interact with the thermally controlled border regions, the total number of atoms in the simulation cell is increased with the recoil energy. Table 5.1 provides the recoil energy values and corresponding numbers of atoms in the simulation cell.

Table 5.1: Simulation parameters. The variable E_{PKA} represents the initial kinetic energy given to PKA, n_{atoms} is the number of atoms in the simulation cell

$E_{\mathrm{PKA}}(eV)$	n_{atoms}
500	81920
750	81920
1000	81920
1500	160000
2000	276480

Periodic boundary conditions were applied in all directions, with a Nosé-Hoover thermostat controlling the temperature along the borders of the simulation cell for mimicking the heat dissipation of bulk materials. The high initial velocities of the PKA decrease over time during cascade simulations. To ensure simulation efficiency and system stability, an adaptive time step was employed. Electrons were not explicitly

modeled in the MD simulations. However, they play a significant role in the energy dissipation during collisions at the energies involved in the studied cascades[48][77]. To account for the energy loss caused by electronic excitations during collisions, a friction term was applied to atoms with kinetic energies above 10 eV in the form of electronic stopping. The simulation time of the single cascades was 50 ps. Approximately 120 simulations were conducted for each recoil energy with varying PKA.

5.2 Analysis Methods

5.2.1 Cluster Analysis

It is fairly common that in the cascades initiated by recoils of keV energies, the defects can agglomerate in defect clusters immediately after the cascade[78]. In the simulation cell, following a cascade, a pair of defects were considered to be part of the same cluster if the distance between them as within a certain cut-off radius. The cut-off radii for interstitial and vacancy clusters are defined in the same way as described in Ref.[79]. Specifically, for interstitial clusters, the cut-off radius is calculated as the average of the distances to the third and fourth nearest neighbors, $r_c^{int} = (r_{3NN} + r_{4NN})/2$. For vacancy clusters, the cut-off radius is computed as the average distance to the second and third nearest neighbors, $r_c^{vac} = (r_{2NN} + r_{3NN})/2$. Here, r_{kNN} is the distance to the kth nearest neighbor. The complex lattice structure of β-Ga_2O_3 makes it challenging to identify its nearest neighbors. To address this issue, we define four nearest distances as follows:

- r_{1NN} as the length of the shortest Ga-O bond,
- r_{2NN} as the shortest O-O distance,
- r_{3NN} as the shortest Ga-Ga distance,
- r_{4NN} as the shortest distance between a Ga ion and an O ion that are bonded together via a single O and Ga ion.

5.3 Defects Formation

Fig. 5.1 presents plots depicting defects formation and temperature variations in single cascade simulations of β-Ga_2O_3 with 1500 eV recoil energy. According to Bacon [80] and Brinkman [81], the development of the cascade can be divided into two distinct phases: collision phase and thermal spike phase (also referred to as the heat spike or displacement spike). During the collision phase, the energy from PKA is distributed among the atoms through collisions, in a chain reaction that leads to displacement of many atoms from their equilibrium positions. With time, the number of displacements

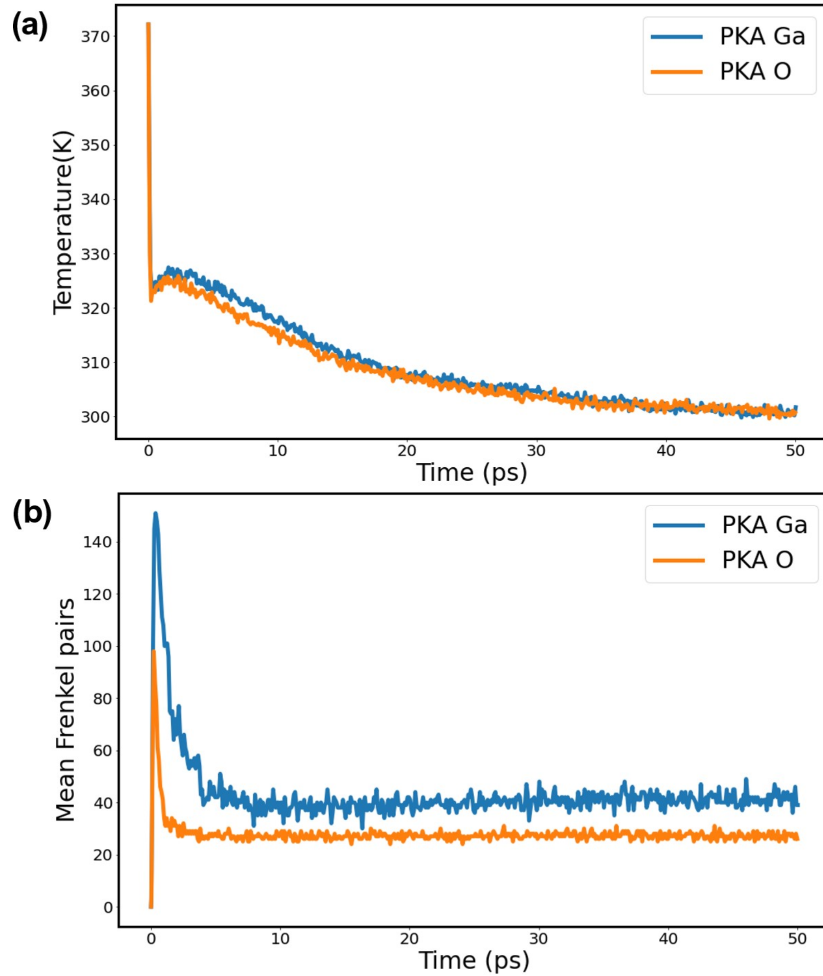

Figure 5.1: Defect-formation and temperature plots for β-Ga_2O_3 1500 eV single cascade MD simulations; (a) shows the temperature change caused by Ga and O PKA in the simulation; (b) shows the amount of Frenkel pairs generated by Ga and O PKA changes respect to time.

increases dramatically, eventually reaching its maximum at approximately 0.3 ps. In dense materials at high recoil energies ($\sim$ a few keV), the initial ballistic phase, i.e. the phase when the energy is transferred from an energetic atom to an atom in rest, can turn into a thermal spike. During such the thermal spike the kinetic energies of atoms involved in it equilibrate and the corresponding region rapidly heats to temperatures above the boiling points for a very short time. The dissipation of energy from a thermal spike proceeds via exciting lattice vibrations (phonons) in the structure. The random thermal motion of atoms leads inevitably to local disorder of a crystal structure, which can be partly or fully recovered or remain disordered (depending on the properties of the material) after the rapid cooling of the thermal spike. The ionic structures have a strong tendency to recrystallization[82] because of strong nature of ionic bonding. In the recrystallization process, which is also referred to as recombination, majority of the displaced atoms return to their regular lattice positions. As the disordered region

regains thermal equilibrium with the bulk at the end of the thermal spike, only a fraction of the initial displacements remain as stable defects. Fig5.1 (b) shows that the collision phase yields a greater quantity of defects when a Ga ion is chosen as a PKA. Nonetheless, in simulations with both Ga and O ions as PKAs, less than 30% of the initial displacements survived after the lattice reached the equilibrium.

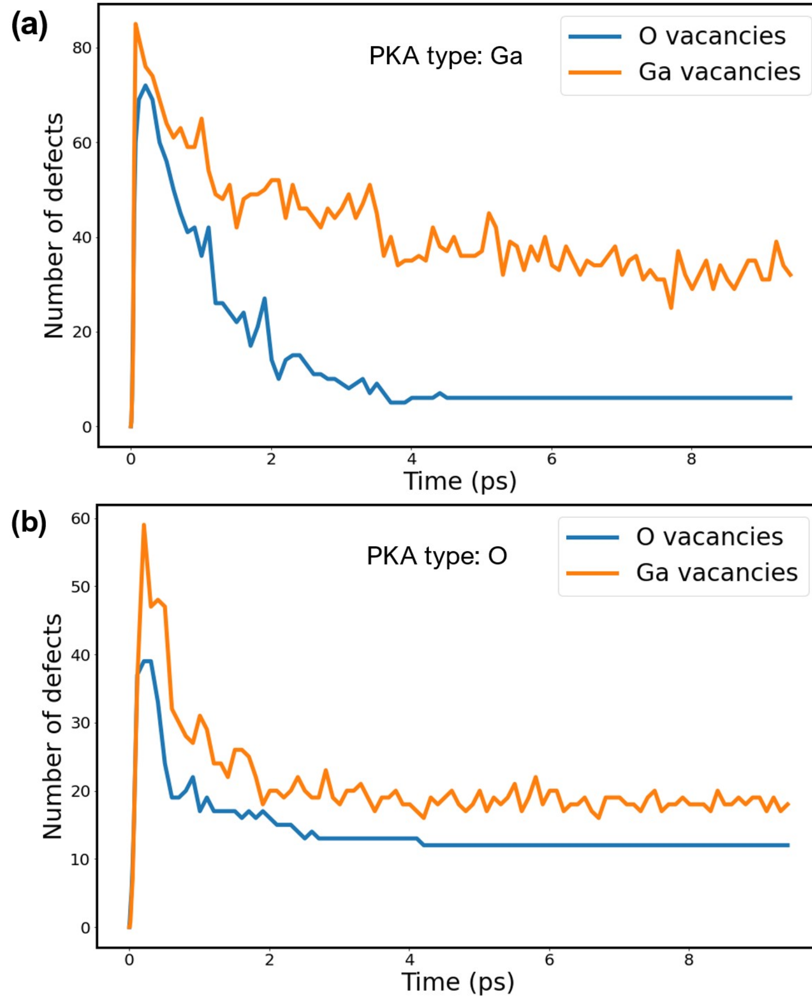

Figure 5.2: Amounts of Ga and O vacancies sites change with time in β-Ga_2O_3 1500 eV single cascade MD simulations, with two types of PKA :(a) Ga ion , (b) O ion.

To comprehensively examine the movements of various defects, Fig. 5.2 illustrates the variation in the quantities of O and Ga vacancy with simulation time for the different PKA types. The simulations with Ga PKAs reveal a slower recombination progress, taking approximately 4 ps to achieve an equilibrium state, compared to the corresponding 2 ps observed in the case of O PKA. Moreover, the maximum number of vacancies in the simulations with the Ga PKAs is higher than that in the O PKA simulations. This phenomenon may be attributed to the fact that Ga PKA is heavier and has larger momentum, enabling it to transfer energy more effectively to surrounding lattice atoms through collisions. Consequently, more atoms are displaced to greater

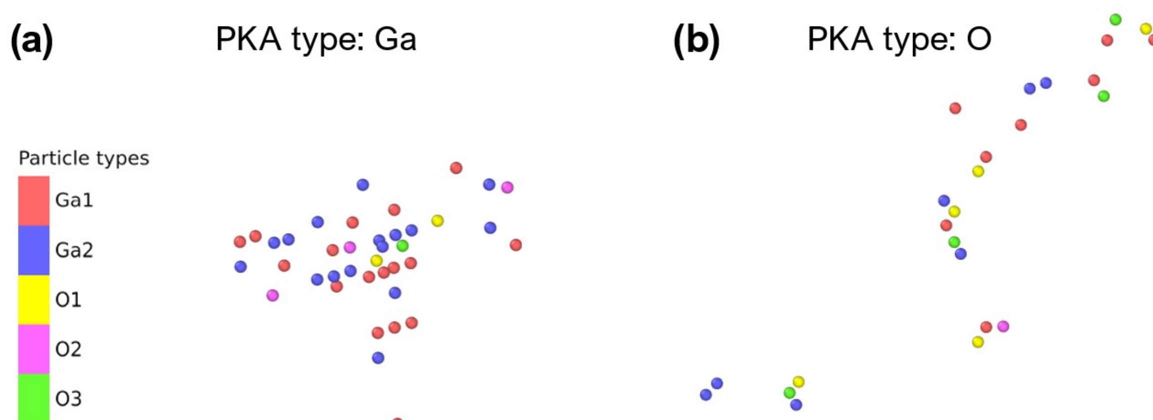

Figure 5.3: The snapshots of vacancies sites at the end of β-Ga_2O_3 single cascade MD simulations in 1500 eV, with two types of PKA:(a) Ga ion , (b) O ion. (The five distinct sites in β-Ga_2O_3 are colored separately. Ga1 sites are shown in red, Ga2 sites are shown in blue, O1 sites are shown in yellow, O2 sites are shown pink, O3 sites are shown in green.))

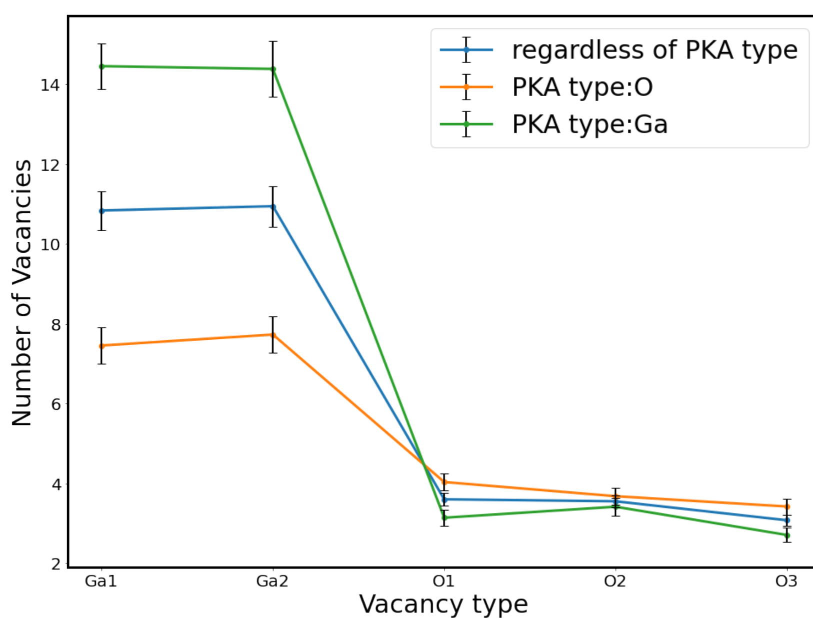

Figure 5.4: Mean number of vacancies with respect to atom's type for β-Ga_2O_3 single cascade MD simulations in 1500 eV

distances from the impact sites and the time for generated defects recovery back to regular lattice is longer. When PKA type is Ga, O vacancies recombined more effectively, reducing from approximately 60 vacancies during the collision phase to less than

10 vacancies. Meanwhile, Ga vacancies decrease from a maximum of approximately 85 to around 40 vacancies. In contrast, the simulations with O PKAs show that Ga and O vacancies exhibit comparable recombination efficiency, with Ga vacancies decreasing from a maximum of 55 to 20 and O vacancies decreasing from a maximum of around 42 to 10 after equilibrium. These results are consistence with the results of Frankel pair simulations discussed in the previous chapter. When Ga is PKA, the majority of knocked Ga ions have displacement distances that are too large to recombine, while O FCC stacking is stable and the knocked-on O ions have strong tendency to recovery. When O is PKA, the displacement distance for both types of ions in the lattice are smaller and most of them tend to recombine to the regular lattice sites.

The final frames were analyzed using the Wigner-Seitz method, Fig. 5.3 displays typical snapshots of the final frames with vacancy sites. When a Ga ion is a PKA, the vacancies tend to form clusters. The vacancy sites in the O PKA simulations are elongated and sparsely distributed. Meanwhile, most vacancies form in the Ga sublattice sites, especially when the PKA is a Ga ion. This finding provides further evidence that an O PKA of the same energy as a Ga PKA moves with higher velocity than the Ga counterpart. It travels to greater distances, while the energy transfer from an O PKA to Ga atoms is less efficient than from a Ga PKA to the Ga ions. Since that it is more difficult to create a Frenkel pair by displacing the O ions (as we saw in the previous chapter), the less efficient energy transfer to Ga ions from an O PKA results in overall lesser number of vacancies produced in the cascades started with an O PKA. The same conclusion can be deduced from Fig. 5.4 , which illustrates the number of vacancies analyzed with respect to the original type of the ion that occupied the vacant site before the cascade. The results are obtained from the statistical analysis of 100 simulations out of which 40 were started with a Ga PKA and 60 with an O PKA. It shows that the amount of O vancany sites generated in Ga PKA simulations is slightly lower than that in O PKA simulations, which is explained by more efficient energy tansfer from the O PKA to a O ion in the lattice to produce a stable O FP. The main factor contributing to the higher production of FPs by the Ga PKAs that is they generated larger amounts of Ga FPs. Also we note that, there are five different atoms types in β-Ga_2O_3. Our simulations show that both Ga1 and Ga2 sites (that indicate that Ga ion to belong in an octahedral or tetrahedral site, respectively) have similar chance to form a vacancy. Similarly, no significant difference is seen for the number of vacancies produced for different types of O atoms. Clearly, the number of bonds per atom does not play dramatic role in FPs formation in β-Ga_2O_3.

5.4 Atoms Mobility

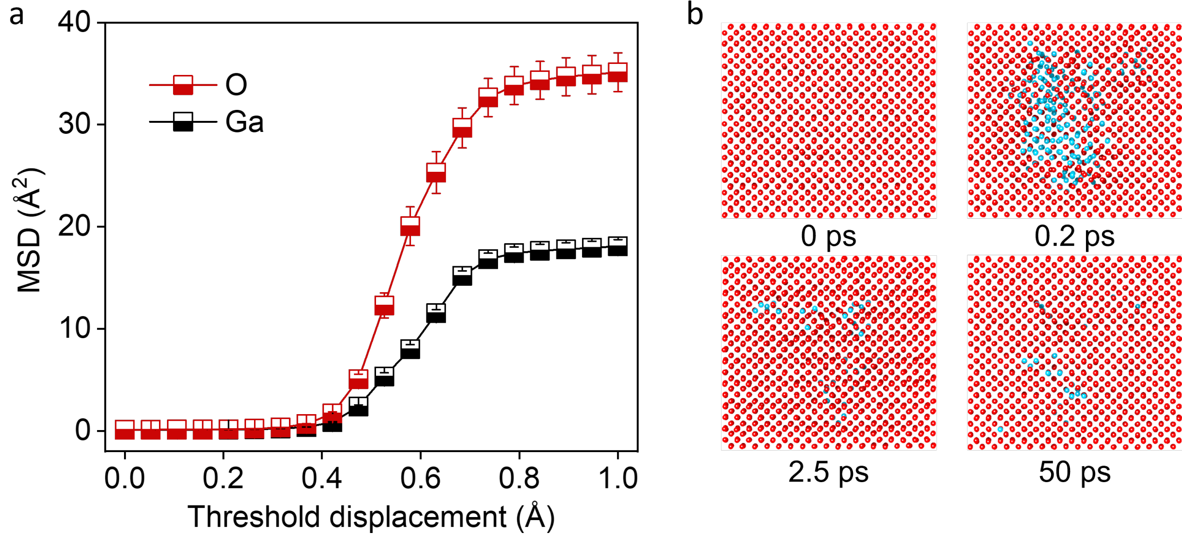

Figure 5.5: a) Mobility of the Ga and O ions during the collision cascades with 1500 eV recoil energy plotted as the mean square displacement (MSD) found from the comparison of the atoms in the first and the last frame after the cascade. The MSD is plotted as a function of the threshold displacement. The error bars are the standard error of the mean collected in 120 MD simulations. b) The snapshots showing the evolution of the oxygen sublattice at different time instances during the cascade. The oxygen ions are colored according to the coordination number (the red color is used for the ions with coordination number ≥ 11, to exclude coloring of atoms around single vacancies, which do not distort the lattice.)

Fig. 5.5 presents an analysis of the stability of the oxygen lattice during collision cascades with 1500 eV recoil energy. The mean square displacement (MSD) for all Ga and O ions that were displaced during the cascades is depicted in Fig5.5 a. By increasing the threshold displacement, which is the minimal displacement distance included in the calculation of MSD, we observe stronger mobility of O ions during the cascades. The red curve displaying the MSD values for O atoms is significantly higher than the blue curve, indicating more efficient displacement of O ions during the cascades. This is also supported by the exemplary snapshots at different time instances of the cascade evolution (0, 0.2, 2.5, and 50 ps), which show the formation of a large number of coordination defects during the cascade that are practically completely eliminated in the O sublattice, leaving only a few vacancy clusters. Given the long time between ion impacts in standard ion accelerators, it is expected that these remaining defects will recover further owing to the strength of the O sublattice, as observed in our simulations.

5.5 Recoil Energy Dependence of Defects

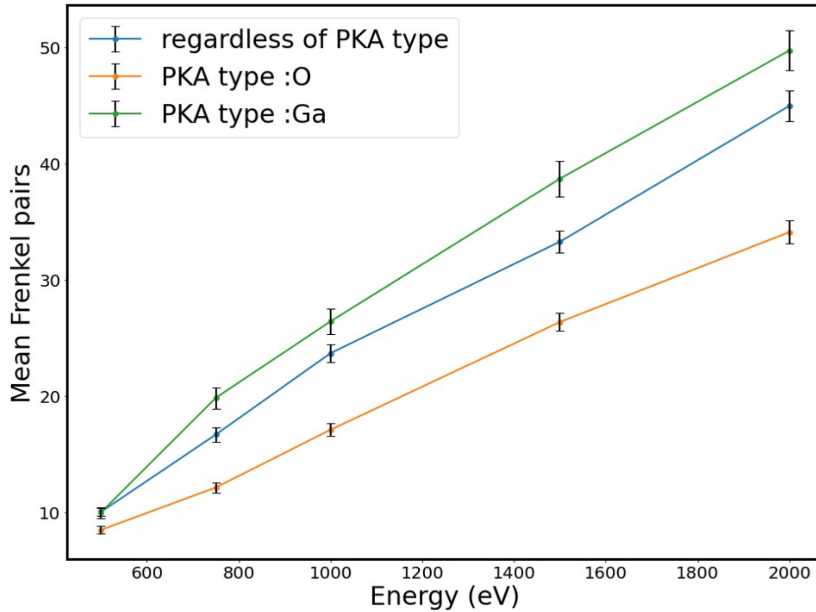

Figure 5.6: Mean number of Frenkel pairs with respect to PKA energy for single cascade MD simulations.

According to the Norgett, Robinson and Torrens (NRT) model[83], the number of defects can be calculated using the following equation.

$$\langle N_{\mathrm{d}}(E) \rangle = \begin{cases} 0, & \text{if } E < E_{\mathrm{d}} \\ 1, & \text{if } E_{\mathrm{d}} \leq E < 2.5E_{\mathrm{d}} \\ \frac{0.8\nu(E)}{2E_{\mathrm{d}}}, & \text{if } 2.5E_{\mathrm{d}} \leq E < \infty \end{cases}$$

Here, $\langle N_{\mathrm{d}}(E) \rangle$ is the number of defects produced by the PKA energy E, $\nu(E)$ is the damage energy which is available to produce a defect and not spent on electronic excitation in the system, and E_{d} is the threshold displacement energy. Fig. 5.6 illustrates the mean number of FPs as a function of PKA energy for both PKA types. The obtained number of the FPs in the simulations of the both types of PKAs is linearly related to the recoil energy, which is consistent with the NRT model. However, the slope of the linear relationship between the number of FPs and recoil energy in the O PKA simulations is smaller than that in the Ga PKA simulations. To elucidate the cause of the observed disparity, we present a detailed breakdown of the types of vacancies generated in each PKA energy simulations, as illustrated in Fig. 5.7. Specifically, we observe a significant increase in the generation of the Ga vacancies in the Ga PKA cascade simulations as compared to the O PKA simulations (Fig. 5.7 a versus b), with the former exhibiting a greater sensitivity to increasing recoil energy. Conversely, we

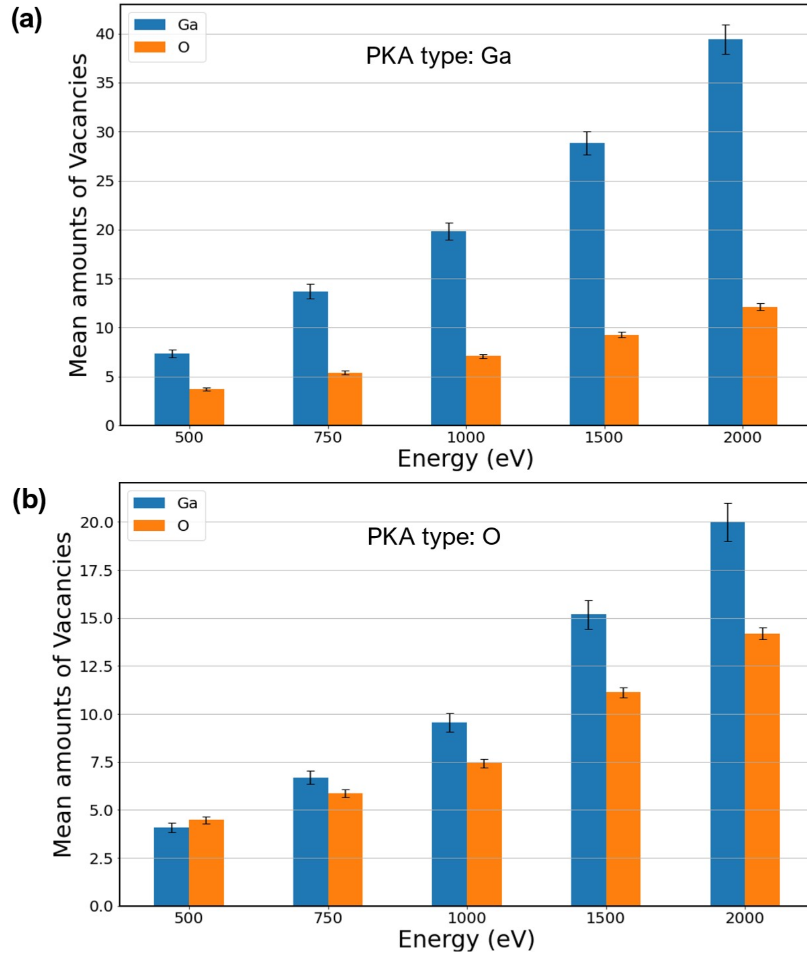

Figure 5.7: Mean number of Ga and O vacancies with respect to PKA energy for single cascade MD simulations, with two types of PKA :(a) Ga ion , (b) O ion

note that O vacancies in both PKA types show only a slight increase with recoil energy. Therefore, we surmise that the primary driver of the observed difference between the defect production in the simulations with both PKA types, is the higher efficiency of the Ga FPs formation in the Ga PKA simulations.

5.6 Defect Clustering

Fig. 5.8 displays the statistical distributions of interstitial and vacancy clusters resulting from 2000 eV cascade MD simulations involving Ga and O PKA. The number of clusters with a size greater than 1 is higher when PKA is Ga ion , which agrees with the observation of vacancy snapshots in Fig. 5.3, indicating that defects tend to aggregate. When O is the PKA, the probability of generating relatively large size clusters is lower. Meanwhile, we use the clustered fraction to assess the clustering efficiency of the formed defects. Clustered fraction is defined as the ratio of the number of defects (vacancies

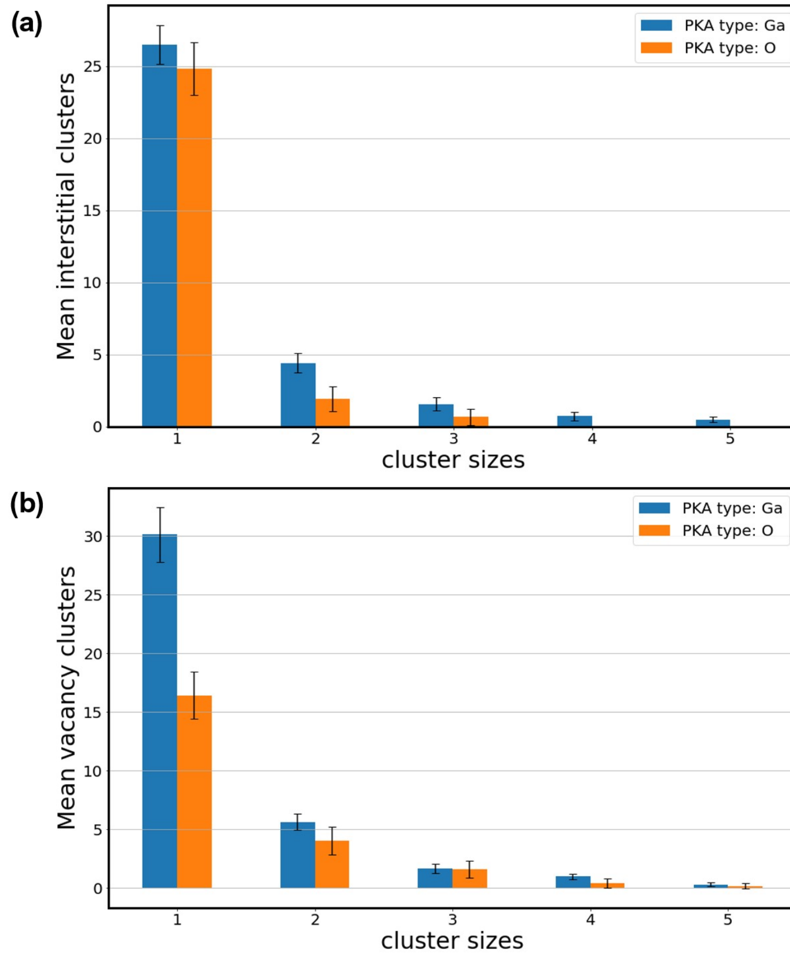

Figure 5.8: Histograms of defect cluster size distributions for 2000 eV single cascade MD simulations with Ga and O PKA :(a) mean number of interstitial clusters with respect to cluster size; (b) mean number of vacancy clusters with respect to cluster size.

or interstitials) bound into clusters with a size greater than one. Fig. 5.9 shows the clustered fraction for both PKA simulations as a function of recoil energy. It could be observed from Fig. 5.9a that the clustered fraction of interstitials is significantly higher in the Ga PKA simulations compared to the O PKA simulations. As depicted in Fig. 5.9b, the difference in the clustered fraction of vacancies between the two simulations is not consistent. This observation could be attributed to the generation of numerous small-size cluster vacancies in the O PKA simulations.

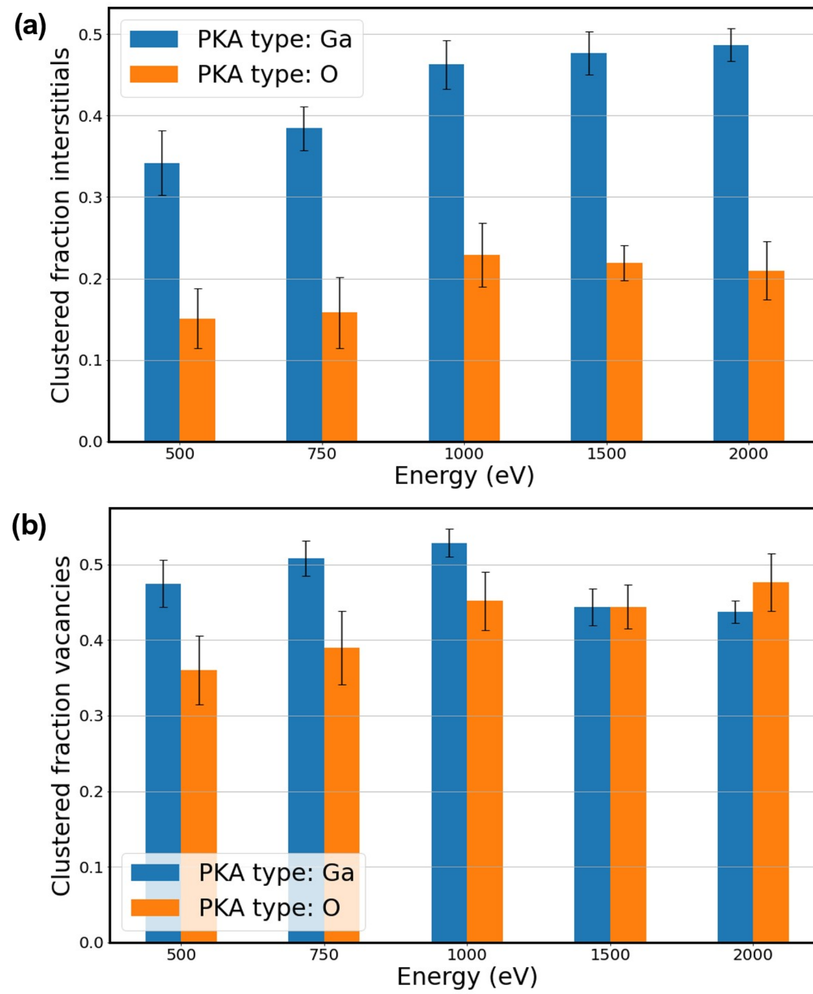

Figure 5.9: Clustered fraction of defects for single cascade MD simulations with Ga and O PKA : (a) clustered fraction interstitials with respect to recoil energy; (b) clustered fraction vacancies with respect to recoil energy.

6. Conclusions

In this thesis, we used molecular dynamic simulations with newly developed machine-learned potentials, tabGAP, to investigate the radiation damage in β-Ga_2O_3. We showed the process of phase transformation from β- to γ-Ga_2O_3 due to accumulation of radiation defects. Our theoretical findings are in a very good agreement with the recent experiments [41] that revealed exceptional radiation tolerance of Ga_2O_3 crystal structure owing to the rich polymorphism of this material. By transforming from the β-Ga_2O_3 to the γ phase under ion implantation, the crystalline structure was able to withstand the damage introduced by 100s of dpa. Moreover, we offered a comprehensive analysis of the stability of Ga and O sublattices in β-Ga_2O_3, and tracked the progress of defect formation under irradiation.

In simulations involving the accumulation of FPs, the introduction of Ga FPs cause the β phase Ga_2O_3 lattice to transform into a phase similar to γ phase, with the degree of similarity strongly dependent on the quantity of Ga FPs. Conversely, if O FPs are introduced, the lattice structure is likely to stay close to its original beta phase. The reason is that FCC stacking O ions are easily recombine in close proximity to their regular lattice sites. Meanwhile, pure type FPs accumulation is unlikely to damage O sublattice sites. However, when Ga and O FPs are implanted simultaneously in the same cell, the O sublattice structure become disordered and the cell transfer to amorphous phase. It appears that Ga interstitial ions act as "damage anchors", preventing later displaced O ions from recombining at the FCC lattice site by altering their surrounding electronic environment. Since the O sublattice in both β- and γ-Ga_2O_3 lattices share the same FCC structure, the experimental finding that β-Ga_2O_3 transfers to the γ phase following ion implantation [41] could be theoretically demonstrated through Ga FPs accumulation simulations. Following the implantation of 200 Ga FPs, the system keeps FCC structure for O sublattice, while containing numerous displaced Ga ions. Upon relaxation, these displaced ions display a structure similar to that of γ-Ga.

Our single cascade MD simulations have revealed a close relationship between defects distributions and PKA type. Specifically, Ga PKA tends to generate more clustered defects, with a higher number of Ga interstitials remaining after recrystallization.

In contrast, O PKA produce sparsely distributed and elongated defects. Although simulations involving O PKA produce a higher number of Ga defects than O defects, the difference in quantity is smaller than when PKA is Ga ion. This is primarily due to the heavier mass of Ga ions, which can transfer their energy to surrounding atoms more effectively through collisions. Consequently, Ga interstitials produced by Ga PKA are displaced further from the collision sites than those resulting from O PKA, resulting in lower recombination efficiency. In the case of the generated O defects, the majority of them tend to revert back to the regular FCC lattice sites and remain similar amounts after both O and Ga PKA cascade simulations. Our mean square displacement analysis revealed that, despite a lower number of O defects in the system, O ions exhibit higher mobility than Ga ions, indicating that O defects are more likely to recover fully due to the stability of the O sublattice. We observed that the number of Ga defects increases linearly with recoil energy, with a higher rate in Ga PKA simulations. On the other hand, the amounts of O defects show a gradual and consistent increase, without any discernible correlation between the PKA type and the rate of increase. Finally, our cluster analysis supports the visualization results, indicating that interstitals have trend to clustered when PKA is Ga ion. The combined findings provide insights into the mechanisms underlying defect generation and recovery in β-Ga_2O_3 during ion implantation, which has significant implications for improving its radiation tolerance, as well as optimizing its electronic and optical properties.

Study of the high doses radiation and investigation of the phase transformation mechanism in Ga_2O_3 using dynamic simulations are highly demanded in the future.

Bibliography

[1] J. Zhao, J. Byggmästar, H. He, K. Nordlund, F. Djurabekova, and M. Hua, "Complex Ga_2O_3 polymorphs explored by accurate and general-purpose machine-learning interatomic potentials," *arXiv preprint arXiv:2212.03096*, 2022.

[2] B. J. Baliga, "Semiconductors for high-voltage, vertical channel field-effect transistors," *Journal of applied Physics*, vol. 53, no. 3, pp. 1759–1764, 1982.

[3] B. J. Baliga, "Power semiconductor device figure of merit for high-frequency applications," *IEEE Electron Device Letters*, vol. 10, no. 10, pp. 455–457, 1989.

[4] S. Pearton, F. Ren, M. Tadjer, and J. Kim, "Perspective: Ga_2O_3 for ultra-high power rectifiers and mosfets," *Journal of Applied Physics*, vol. 124, no. 22, p. 220901, 2018.

[5] S. Pearton, J. Yang, P. H. Cary IV, F. Ren, J. Kim, M. J. Tadjer, and M. A. Mastro, "A review of Ga_2O_3 materials, processing, and devices," *Applied Physics Reviews*, vol. 5, no. 1, p. 011301, 2018.

[6] H. He, R. Orlando, M. A. Blanco, R. Pandey, E. Amzallag, I. Baraille, and M. Rérat, "First-principles study of the structural, electronic, and optical properties of Ga_2O_3 in its monoclinic and hexagonal phases," *Physical Review B*, vol. 74, no. 19, p. 195123, 2006.

[7] S. Yoshioka, H. Hayashi, A. Kuwabara, F. Oba, K. Matsunaga, and I. Tanaka, "Structures and energetics of Ga_2O_3 polymorphs," *Journal of Physics: Condensed Matter*, vol. 19, no. 34, p. 346211, 2007.

[8] M. Marezio and J. Remeika, "Bond lengths in the α-Ga_2O_3 structure and the high-pressure phase of $Ga_{2-x}Fe_xO_3$," *The Journal of Chemical Physics*, vol. 46, no. 5, pp. 1862–1865, 1967.

[9] J. Kohn, G. Katz, and J. Broder, "Characterization of β-Ga_2O_3 and its alumina isomorph, θ-Al_2O_3," *American Mineralogist: Journal of Earth and Planetary Materials*, vol. 42, no. 5-6, pp. 398–407, 1957.

[10] P. Kroll, R. Dronskowski, and M. Martin, "Formation of spinel-type gallium oxynitrides: a density-functional study of binary and ternary phases in the system Ga–O–N," *Journal of Materials Chemistry*, vol. 15, no. 32, pp. 3296–3302, 2005.

[11] S. Stepanov, V. Nikolaev, V. Bougrov, and A. Romanov, "Gallium oxide: Properties and applica 498 a review," *Rev. Adv. Mater. Sci*, vol. 44, pp. 63–86, 2016.

[12] Y. Arata, H. Nishinaka, D. Tahara, and M. Yoshimoto, "van der waals epitaxy of ferroelectric ε-gallium oxide thin film on flexible synthetic mica," *Japanese Journal of Applied Physics*, vol. 59, no. 2, p. 025503, 2020.

[13] R. Roy, V. Hill, and E. Osborn, "Polymorphism of Ga_2O_3 and the system Ga_2O_3-H_2O," *Journal of the American Chemical Society*, vol. 74, no. 3, pp. 719–722, 1952.

[14] H. Y. Playford, A. C. Hannon, E. R. Barney, and R. I. Walton, "Structures of uncharacterised polymorphs of gallium oxide from total neutron diffraction," *Chemistry–A European Journal*, vol. 19, no. 8, pp. 2803–2813, 2013.

[15] I. Cora, F. Mezzadri, F. Boschi, M. Bosi, M. Čaplovičová, G. Calestani, I. Dódony, B. Pécz, and R. Fornari, "The real structure of ε-Ga_2O_3 and its relation to κ-phase," *CrystEngComm*, vol. 19, no. 11, pp. 1509–1516, 2017.

[16] M. Kneiß, A. Hassa, D. Splith, C. Sturm, H. Von Wenckstern, T. Schultz, N. Koch, M. Lorenz, and M. Grundmann, "Tin-assisted heteroepitaxial PLD-growth of κ-Ga_2O_3 thin films with high crystalline quality," *APL Materials*, vol. 7, no. 2, p. 022516, 2019.

[17] J. Kim, D. Tahara, Y. Miura, and B. G. Kim, "First-principle calculations of electronic structures and polar properties of (κ, ε)-Ga_2O_3," *Applied Physics Express*, vol. 11, no. 6, p. 061101, 2018.

[18] S. Geller, "Crystal structure of β-Ga_2O_3," *The Journal of Chemical Physics*, vol. 33, no. 3, pp. 676–684, 1960.

[19] S. Geller, "On the structure of β-Ga_2O_3," *Journal of Solid State Chemistry*, vol. 20, no. 2, pp. 209–210, 1977.

[20] M. J. Tadjer, J. L. Lyons, N. Nepal, J. A. Freitas, A. D. Koehler, and G. M. Foster, "Review-theory and characterization of doping and defects in β-Ga_2O_3," *ECS Journal of Solid State Science and Technology*, vol. 8, no. 7, pp. Q3187–Q3194, 2019.

[21] E. Ahmadi, O. S. Koksaldi, S. W. Kaun, Y. Oshima, D. B. Short, U. K. Mishra, and J. S. Speck, "Ge doping of β-Ga_2O_3 films grown by plasma-assisted molecular beam epitaxy," *Applied Physics Express*, vol. 10, no. 4, p. 041102, 2017.

[22] M. Higashiwaki, K. Sasaki, H. Murakami, Y. Kumagai, A. Koukitu, A. Kuramata, T. Masui, and S. Yamakoshi, "Recent progress in Ga_2O_3 power devices," *Semiconductor Science and Technology*, vol. 31, no. 3, p. 034001, 2016.

[23] J. L. Lyons, "A survey of acceptor dopants for β-Ga_2O_3," *Semiconductor science and technology*, vol. 33, no. 5, p. 05LT02, 2018.

[24] J. B. Varley, J. R. Weber, A. Janotti, and C. G. Van de Walle, "Oxygen vacancies and donor impurities in β-Ga_2O_3," *Applied Physics Letters*, vol. 97, no. 14, p. 142106, 2010.

[25] Y. K. Frodason, K. Johansen, L. Vines, and J. Varley, "Self-trapped hole and impurity-related broad luminescence in β-Ga_2O_3," *Journal of Applied Physics*, vol. 127, no. 7, p. 075701, 2020.

[26] J. Srour and J. Palko, "A framework for understanding displacement damage mechanisms in irradiated silicon devices," *IEEE transactions on nuclear science*, vol. 53, no. 6, pp. 3610–3620, 2006.

[27] J. Nord, K. Nordlund, and J. Keinonen, "Molecular dynamics study of damage accumulation in GaN during ion beam irradiation," *Physical Review B*, vol. 68, no. 18, p. 184104, 2003.

[28] S. Pearton, Y.-S. Hwang, and F. Ren, "Radiation effects in gan-based high electron mobility transistors," *Jom*, vol. 67, pp. 1601–1611, 2015.

[29] A. Y. Polyakov, S. Pearton, P. Frenzer, F. Ren, L. Liu, and J. Kim, "Radiation effects in GaN materials and devices," *Journal of Materials Chemistry C*, vol. 1, no. 5, pp. 877–887, 2013.

[30] X. Xia, J.-S. Li, R. Sharma, F. Ren, M. A. J. Rasel, S. Stepanoff, N. Al-Mamun, A. Haque, D. E. Wolfe, S. Modak, *et al.*, "Radiation damage in the ultra-wide bandgap semiconductor Ga_2O_3," *ECS Journal of Solid State Science and Technology*, vol. 11, no. 9, p. 095001, 2022.

[31] N. Manikanthababu, H. Sheoran, P. Siddham, and R. Singh, "Review of radiation-induced effects on β-Ga_2O_3 materials and devices," *Crystals*, vol. 12, no. 7, p. 1009, 2022.

[32] J. Yang, C. Fares, Y. Guan, F. Ren, S. Pearton, J. Bae, J. Kim, and A. Kuramata, "Eighteen mega-electron-volt alpha-particle damage in homoepitaxial β-Ga_2O_3 schottky rectifiers," *Journal of Vacuum Science & Technology B, Nanotechnology and Microelectronics: Materials, Processing, Measurement, and Phenomena*, vol. 36, no. 3, p. 031205, 2018.

[33] E. Farzana, M. F. Chaiken, T. E. Blue, A. R. Arehart, and S. A. Ringel, "Impact of deep level defects induced by high energy neutron radiation in β-Ga_2O_3," *APL Materials*, vol. 7, no. 2, p. 022502, 2019.

[34] S. Ahn, Y.-H. Lin, F. Ren, S. Oh, Y. Jung, G. Yang, J. Kim, M. A. Mastro, J. K. Hite, C. R. Eddy Jr, *et al.*, "Effect of 5 mev proton irradiation damage on performance of β-Ga_2O_3 photodetectors," *Journal of Vacuum Science & Technology B, Nanotechnology and Microelectronics: Materials, Processing, Measurement, and Phenomena*, vol. 34, no. 4, p. 041213, 2016.

[35] D. Kaur, P. Vashishtha, S. A. Khan, P. K. Kulriya, G. Gupta, and M. Kumar, "Phase dependent radiation hardness and performance analysis of amorphous and polycrystalline Ga_2O_3 solar-blind photodetector against swift heavy ion irradiation," *Journal of Applied Physics*, vol. 128, no. 6, p. 065902, 2020.

[36] J. Kim, S. J. Pearton, C. Fares, J. Yang, F. Ren, S. Kim, and A. Y. Polyakov, "Radiation damage effects in Ga_2O_3 materials and devices," *Journal of Materials Chemistry C*, vol. 7, no. 1, pp. 10–24, 2019.

[37] T. Wang, S. S. Farvid, M. Abulikemu, and P. V. Radovanovic, "Size-tunable phosphorescence in colloidal metastable γ-Ga_2O_3 nanocrystals," *Journal of the American Chemical Society*, vol. 132, no. 27, pp. 9250–9252, 2010.

[38] D. Machon, P. F. McMillan, B. Xu, and J. Dong, "High-pressure study of the β-to-α transition in Ga_2O_3," *Physical Review B*, vol. 73, no. 9, p. 094125, 2006.

[39] Y. Xu, J.-H. Park, Z. Yao, C. Wolverton, M. Razeghi, J. Wu, and V. P. Dravid, "Strain-induced metastable phase stabilization in Ga_2O_3 thin films," *ACS applied materials & interfaces*, vol. 11, no. 5, pp. 5536–5543, 2019.

[40] E. A. Anber, D. Foley, A. C. Lang, J. Nathaniel, J. L. Hart, M. J. Tadjer, K. D. Hobart, S. Pearton, and M. L. Taheri, "Structural transition and recovery of ge implanted β-Ga_2O_3," *Applied Physics Letters*, vol. 117, no. 15, p. 152101, 2020.

[41] A. Azarov, J. G. Fernández, J. Zhao, F. Djurabekova, H. He, R. He, Ø. Prytz, L. Vines, U. Bektas, P. Chekhonin, *et al.*, "Universal radiation tolerant semiconductor," *arXiv preprint arXiv:2303.13114*, 2023.

[42] E. Wendler, E. Treiber, J. Baldauf, S. Wolf, and C. Ronning, "High-level damage saturation below amorphisation in ion implanted β-Ga_2O_3," *Nuclear Instruments and Methods in Physics Research Section B: Beam Interactions with Materials and Atoms*, vol. 379, pp. 85–90, 2016.

[43] A. Nikolskaya, E. Okulich, D. Korolev, A. Stepanov, D. Nikolichev, A. Mikhaylov, D. Tetelbaum, A. Almaev, C. A. Bolzan, A. Buaczik Jr, *et al.*, "Ion implantation in β-Ga_2O_3: Physics and technology," *Journal of Vacuum Science & Technology A: Vacuum, Surfaces, and Films*, vol. 39, no. 3, p. 030802, 2021.

[44] B. L. Aarseth, C. S. Granerød, A. Galeckas, A. Azarov, P. D. Nguyen, Ø. Prytz, and L. Vines, "Formation and functionalization of Ge-nanoparticles in ZnO," *Nanotechnology*, vol. 32, no. 50, p. 505707, 2021.

[45] A. Meldrum, J. Haglund, RF, L. A. Boatner, and C. W. White, "Nanocomposite materials formed by ion implantation," *Advanced Materials*, vol. 13, no. 19, pp. 1431–1444, 2001.

[46] J. García-Fernández, S. Kjeldby, P. Nguyen, O. Karlsen, L. Vines, and Ø. Prytz, "Formation of γ-Ga_2O_3 by ion implantation: Polymorphic phase transformation of β-Ga_2O_3," *Applied Physics Letters*, vol. 121, no. 19, p. 191601, 2022.

[47] A. Hamedani, J. Byggmästar, F. Djurabekova, G. Alahyarizadeh, R. Ghaderi, A. Minuchehr, and K. Nordlund, "Primary radiation damage in silicon from the viewpoint of a machine learning interatomic potential," *Physical Review Materials*, vol. 5, no. 11, p. 114603, 2021.

[48] K. Nordlund, S. J. Zinkle, A. E. Sand, F. Granberg, R. S. Averback, R. E. Stoller, T. Suzudo, L. Malerba, F. Banhart, W. J. Weber, *et al.*, "Primary radiation damage: A review of current understanding and models," *Journal of Nuclear Materials*, vol. 512, pp. 450–479, 2018.

[49] S. Zinkle and C. Kinoshita, "Defect production in ceramics," *Journal of Nuclear Materials*, vol. 251, pp. 200–217, 1997.

[50] R. Stoller, "1.11-primary radiation damage formation," *Comprehensive nuclear materials*, pp. 293–332, 2012.

[51] T. D. De La Rubia, R. S. Averback, R. Benedek, and W. King, "Role of thermal spikes in energetic displacement cascades," *Physical review letters*, vol. 59, no. 17, p. 1930, 1987.

[52] A. E. Stuchbery and E. Bezakova, "Thermal-spike lifetime from picosecond-duration preequilibrium effects in hyperfine magnetic fields following ion implantation," *Physical review letters*, vol. 82, no. 18, p. 3637, 1999.

[53] J. M. Ziman, *Principles of the Theory of Solids*. Cambridge university press, 1972.

[54] J. Gibson, A. N. Goland, M. Milgram, and G. Vineyard, "Dynamics of radiation damage," *Physical Review*, vol. 120, no. 4, p. 1229, 1960.

[55] J. W. Christian, *The theory of transformations in metals and alloys*. Newnes, 2002.

[56] K. Nordlund, M. Ghaly, R. Averback, M. Caturla, T. D. de La Rubia, and J. Tarus, "Defect production in collision cascades in elemental semiconductors and fcc metals," *Physical Review B*, vol. 57, no. 13, p. 7556, 1998.

[57] J. Friedel, *Dislocations: international series of monographs on solid state physics*, vol. 3. Elsevier, 2013.

[58] Z. Rong, V. Mohles, D. J. Bacon*, and Y. N. Osetsky, "Dislocation dynamics modelling of dislocation–loop interactions in irradiated metals," *Philosophical Magazine*, vol. 85, no. 2-3, pp. 171–188, 2005.

[59] A. Breidi and S. Dudarev, "Dislocation dynamics simulation of thermal annealing of a dislocation loop microstructure," *Journal of Nuclear Materials*, vol. 562, p. 153552, 2022.

[60] W.-Y. Chen, Y. Miao, J. Gan, M. A. Okuniewski, S. A. Maloy, and J. F. Stubbins, "Neutron irradiation effects in Fe and Fe-Cr at 300 c," *Acta Materialia*, vol. 111, pp. 407–416, 2016.

[61] I. L. Garzon and A. Posada-Amarillas, "Structural and vibrational analysis of amorphous Au 55 clusters," *Physical Review B*, vol. 54, no. 16, p. 11796, 1996.

[62] K. Nordlund and R. Averback, "Point defect movement and annealing in collision cascades," *Physical Review B*, vol. 56, no. 5, p. 2421, 1997.

[63] K. Nordlund and F. Djurabekova, "Multiscale modelling of irradiation in nanostructures," *Journal of Computational Electronics*, vol. 13, pp. 122–141, 2014.

[64] W. C. Swope, H. C. Andersen, P. H. Berens, and K. R. Wilson, "A computer simulation method for the calculation of equilibrium constants for the formation of physical clusters of molecules: Application to small water clusters," *The Journal of chemical physics*, vol. 76, no. 1, pp. 637–649, 1982.

[65] K. Nordlund, "Molecular dynamics simulation of ion ranges in the 1–100 kev energy range," *Computational materials science*, vol. 3, no. 4, pp. 448–456, 1995.

[66] M. Tuckerman, B. J. Berne, and G. J. Martyna, "Reversible multiple time scale molecular dynamics," *The Journal of chemical physics*, vol. 97, no. 3, pp. 1990–2001, 1992.

[67] S. Nosé, "A unified formulation of the constant temperature molecular dynamics methods," *The Journal of chemical physics*, vol. 81, no. 1, pp. 511–519, 1984.

[68] X. Wang, S. Ramírez-Hinestrosa, J. Dobnikar, and D. Frenkel, "The lennard-jones potential: when (not) to use it," *Physical Chemistry Chemical Physics*, vol. 22, no. 19, pp. 10624–10633, 2020.

[69] X. Zhu, P. E. Lopes, and A. D. MacKerell Jr, "Recent developments and applications of the charmm force fields," *Wiley Interdisciplinary Reviews: Computational Molecular Science*, vol. 2, no. 1, pp. 167–185, 2012.

[70] J. Wang, R. M. Wolf, J. W. Caldwell, P. A. Kollman, and D. A. Case, "Development and testing of a general amber force field," *Journal of computational chemistry*, vol. 25, no. 9, pp. 1157–1174, 2004.

[71] F. Granberg, K. Nordlund, M. W. Ullah, K. Jin, C. Lu, H. Bei, L. Wang, F. Djurabekova, W. Weber, and Y. Zhang, "Mechanism of radiation damage reduction in equiatomic multicomponent single phase alloys," *Physical review letters*, vol. 116, no. 13, p. 135504, 2016.

[72] S. Plimpton, "Fast parallel algorithms for short-range molecular dynamics," *Journal of computational physics*, vol. 117, no. 1, pp. 1–19, 1995.

[73] D. L. Ermak and J. A. McCammon, "Brownian dynamics with hydrodynamic interactions," *The Journal of chemical physics*, vol. 69, no. 4, pp. 1352–1360, 1978.

[74] J. L. Yarnell, M. Katz, R. G. Wenzel, and S. Koenig, "Structure factor and radial distribution function for liquid argon at 85 k," *Physical Review A*, vol. 7, no. 6, p. 2130, 1973.

[75] P. Zou and R. Bader, "A topological definition of a wigner–seitz cell and the atomic scattering factor," *Acta Crystallographica Section A: Foundations of Crystallography*, vol. 50, no. 6, pp. 714–725, 1994.

[76] A. Stukowski, "Visualization and analysis of atomistic simulation data with ovito– the open visualization tool," *Modelling and simulation in materials science and engineering*, vol. 18, no. 1, p. 015012, 2009.

[77] J. F. Ziegler and J. P. Biersack, *The stopping and range of ions in matter*. Springer, 1985.

[78] R. E. Stoller, "The role of cascade energy and temperature in primary defect formation in iron," *Journal of nuclear materials*, vol. 276, no. 1-3, pp. 22–32, 2000.

[79] J. Byggmästar, F. Granberg, and K. Nordlund, "Effects of the short-range repulsive potential on cascade damage in iron," *Journal of Nuclear Materials*, vol. 508, pp. 530–539, 2018.

[80] D. J. Bacon and T. D. De La Rubia, "Molecular dynamics computer simulations of displacement cascades in metals," *Journal of Nuclear Materials*, vol. 216, pp. 275–290, 1994.

[81] J. A. Brinkman, "On the nature of radiation damage in metals," *Journal of Applied Physics*, vol. 25, no. 8, pp. 961–970, 1954.

[82] C. Kittel and P. McEuen, *Introduction to solid state physics*. John Wiley & Sons, 2018.

[83] M. Norgett, M. Robinson, and I. M. Torrens, "A proposed method of calculating displacement dose rates," *Nuclear engineering and design*, vol. 33, no. 1, pp. 50–54, 1975.